AD-A034 054

ROCKET INFRARED SPECTROSCOPY OF THE ZODIACAL DUST CLOUD

CORNELL UNIVERSITY, ITHACA, NEW YORK

1 OCTOBER 1976

011102

AFGL-TR-76-0236

ROCKET INFRARED SPECTROSCOPY OF
THE ZODIACAL DUST CLOUD

Daniel A. Briotta, Jr.
Judith L. Pipher
James R. Houck

Cornell University
Center for Radiophysics & Space Research
Ithaca, New York 14353

Final Report
1 May 1973 - 1 January 1976

D D C
JAN 6 1977
RECEIVED
C

1 October 1976

Approved for public release; distribution unlimited

This research has been sponsored by Defense Advanced Research
Projects Agency, ARPA Order No. 1366

AIR FORCE GEOPHYSICS LABORATORY
AIR FORCE SYSTEMS COMMAND
UNITED STATES AIR FORCE
HANSCOM AFB, MASSACHUSETTS 01731

Qualified requestors may obtain additional copies from the
Defense Documentation Center. All others should apply to
the National Technical Information Service.

SECURITY CLASSIFICATION OF THIS PAGE (When Data Entered)

REPORT DOCUMENTATION PAGE		READ INSTRUCTIONS BEFORE COMPLETING FORM
1. REPORT NUMBER AFGL-TR-76-0236	2. GOVT ACCESSION NO.	3. RECIPIENT'S CATALOG NUMBER
4. TITLE (and Subtitle) ROCKET INFRARED SPECTROSCOPY OF THE ZODIACAL DUST CLOUD		5. TYPE OF REPORT & PERIOD COVERED Final Report 1 May 1973 - 1 Jan 1976
		6. PERFORMING ORG. REPORT NUMBER
7. AUTHOR(s) Daniel A. Briotta, Jr. Judith L. Pipher James R. Houck		8. CONTRACT OR GRANT NUMBER(s) F19628-73-C-0242
9. PERFORMING ORGANIZATION NAME AND ADDRESS Cornell University Center for Radiophysics & Space Research Ithaca, New York 14853		10. PROGRAM ELEMENT, PROJECT, TASK AREA & WORK UNIT NUMBERS 62301E P, T&WU n/a ARPA 1366
11. CONTROLLING OFFICE NAME AND ADDRESS Air Force Geophysics Laboratory Hanscom AFB, Massachusetts 01731 Monitor/Thomas L. Murdock, Capt, USAF/OPI		12. REPORT DATE 1 October 1976
		13. NUMBER OF PAGES 95
14. MONITORING AGENCY NAME & ADDRESS(if different from Controlling Office)		15. SECURITY CLASS. (of this report) Unclassified
		15a. DECLASSIFICATION/DOWNGRADING SCHEDULE

16. DISTRIBUTION STATEMENT (of this Report)

Approved for public release; distribution unlimited.

17. DISTRIBUTION STATEMENT (of the abstract entered in Block 20, if different from Report)

19. KEY WORDS (Continue on reverse side if necessary and identify by block number)

Infrared
Zodiacal dust
Silicate dust

20. ABSTRACT (Continue on reverse side if necessary and identify by block number)

The 8-14μ infrared spectrum of the zodiacal dust cloud has been measured with a resolution of $\Delta\lambda/\lambda \sim 0.03$. The observations were made with a liquid helium cooled array spectrometer and telescope from an altitude of ~ 300km. The design, testing, and calibration of the rocket payload are described.

Technical problems occurred during the flight that destroyed ~ 90 percent of the data. However, one good scan across the ecliptic plane at a solar

DD FORM 1 JAN 73 1473   EDITION OF 1 NOV 65 IS OBSOLETE

elongation of $\sim 103^{\circ}$ was obtained. The intensity near the ecliptic is $\sim 6.6 \times 10^{-11}$ watts/cm^2 srμ. The spectrum shows a pronounced silicate emission feature similar to that seen in carbonaceous chondrites and in the Orion Nebula, along with a dilute underlying blackbody.

ROCKET INFRARED SPECTROSCOPY OF THE ZODIACAL DUST CLOUD

Daniel A. Briotta, Jr., J.L. Pipher[*] and J.R. Houck
Cornell University, 1976

The 8-14μ infrared spectrum of the zodiacal dust cloud has been measured with a resolution of $\Delta\lambda/\lambda \sim 0.03$. The observations were made with a liquid helium cooled array spectrometer and telescope from an altitude of $\sim$ 300km. The design, testing, and calibration of the rocket payload are described.

Technical problems occurred during the flight that destroyed $\sim$ 90% of the data. However, one good scan across the ecliptic plane at a solar elongation of $\sim 103^{\circ}$ was obtained. The intensity near the ecliptic is $\sim 6.6 \times 10^{-11}$ watts/cm^{2}srμ. The spectrum shows a pronounced silicate emission feature similar to that seen in carbonaceous chondrites and in the Orion Nebula, along with a dilute underlying blackbody.

The shape of the silicate feature indicates a typical grain size of the order of 5μ, although larger blackbody grains and possibly smaller, hotter silicate grains may also contribute to the emission. The dilutions are consistent with the particle and mass densities observed by

---

[*]Permanent address: Department of Physics and Astronomy
University of Rochester, Rochester, New York

iii

consistent with the particle and mass densities observed by spacecraft. The temperatures are reasonable for the blackbody grains (T ~ 300°K), but require a strong green-house effect for the smaller particles producing the silicate feature (T ~ 375°K). The presence of the 10μ silicate band suggests that observations of the 18μ band are possible, and may help identify the mineralogical nature of the grain material.

TABLE OF CONTENTS

TABLE OF CONTENTS (cont'd)

LIST OF TABLES

LIST OF FIGURES

CHAPTER I

Introduction

The infrared spectra of silicate material is char-
acterized by strong features at wavelengths of 10 and 18
microns. The first is due to transitions between Si-O
stretching modes, and the latter to Si-O-Si bending modes.
The feature at 10 microns is somewhat stronger and has
been seen in many astrophysical sources. This thesis re-
ports the results of a search for a similar emission fea-
ture in the Zodiacal dust cloud.

The arguments for the presence of silicate material
in the zodiacal dust are strong. The existence of the
Gegenschein, a back-scattering effect, requires the scat-
tering particles to be mainly dielectrics (Leinert, 1975).
Considerations of the grains' origins also suggest sili-
cates.

There are two common theories for the dust's origin.
One is that the grains are injected from the asteroid belt
where they are created by collisions and fragmentation.
The other view is that comet tails supply the dust. The
first theory is gaining favor as a result of recent space-
craft measurements by the Pioneers and Mariners (see below).
However the long lifetime of a typical dust particle in the
cloud ($\sim 10^4$ yr for a 1μ grain, Leinert, 1975) compared to
the injection rate from the dust tails of comets implies

that comets could supply a significant portion of the particles.

Regardless of the source, it seems likely that silicates make up a large fraction of the grain material. They are seen in both comets and meteorites. Ney (1974) found excess emission at 10 microns in the coma and tail of comet Kohoutek, but no excess in the anti-tail, which he attributed to the presence of larger silicate grains on the basis of dynamical effects and silicate opacities (see below). He also found excesses at 10 microns in comets Bennet and Bradfield. Merrill (1974) measured the 8-13 micron spectrum of Kohoutek and found the emission feature to resemble closely that seen in the circumstellar dust in the Orion Nebula and attributed to silicate material. In turn, Zaikowski and Knacke (1975) have found that the spectra of carbonaceous chondrites are similar to the absorption feature in Orion, and that the similarities are greater for the Type I meteorite Orgueil, where most of the silicate is in hydrous form, than for the Type II's, which contain fragments of olivine and pyroxene. This is significant because the Type I meteorites are believed to contain unprocessed primitive material from the early solar nebula. Comets and asteroids may be repositories of such primitive material. As sources for the zodiacal dust, this would imply a similar composition for the grains.

Whether the 10 micron silicate feature is observable

or not, however, depends on the size distribution of the grains and, to some extent, on the spatial distribution. Most models of the cloud have assumed a power law distribution in the form $n(a,r) \propto a^{-k}r^{-p}$, where a is the grain radius, and r the distance from the sun. If k is small, i.e. ≤ 2, then emission from large optically thick grains will dominate, and the silicate feature will be unobservable without extremely accurate measurements.

To estimate the effect of grain size on the visibility of the silicate feature, I have assumed a typical opacity for small silicate grains to be $\kappa \sim 10^3$ cm^2/gm and a typical density of $\rho \sim 3$ gm/cm^3, following Ney (1974). For small spherical particles, the optical depth may be written $\tau_\lambda = \frac{4}{3} a \kappa_\lambda \rho$. At a wavelength of 10 microns, the grain would become optically thick for $a \sim 2.5\mu$. For wavelengths between 8 and 13 microns, the relative opacity can be estimated from the data of Gillett et al. (1975) on the silicate emission feature seen in the Trapezium region of the Orion Nebula. This type of grain will be optically thin at 13 microns for radii less than $a \sim 7.5\mu$, and at 8 microns for $a \leq 9.8\mu$. For typical photometric accuracies of 5 to 10%, deviations from blackbody emission between 8 and 13 microns should be detectable from a grain whose optical depth at 13 microns is less than $\tau \leq 2-3$. Since the opacity at 13 microns is about 1/3 that at 10 microns for Trapezium-like grains, deviations from blackbody emission should be detectable for $a \leq 15-20\mu$ in these grains, provided that

grains larger than this are not sufficiently abundant to wash out the feature.

Information about the size and spatial distributions of the grains comes primarily from optical studies of the zodiacal light, and, more recently, from balloon, rocket, and spacecraft observations. These will now be discussed with a view towards what they can tell us about the distributions.

Ground-based observations of the zodiacal light (e.g. Weinberg, 1964; and Wolstencroft and Rose, 1967) are hampered by the fact that they must usually be made when the sky is fairly bright. Corrections for atmospheric emission are fairly large, and early measurements tended to give significantly different results. Recent calculations of the Mie-scattering component in the earth's atmosphere (Staude, 1975) are beginning to make the measurements more consistent. Measurements are also becoming available from balloon altitudes, which avoid much of the atmospheric corrections of ground-based studies, and from rockets and satellites which avoid the atmosphere entirely.

These measurements have shown the intensity of scattered sunlight to vary approximately as $I(\epsilon) \propto \epsilon^{-2.2}$, where ϵ is the elongation from the sun. However for elongations greater than 160-170° there is an increase in intensity, due to backscattering, called the Gegenschein. Except for the Gegenschein, which is always found at the antisolar point, the emission is symmetric about the invariant

plane of the solar system to within about 2° (Dumont and Sanchez, 1975; Robley, 1975). Perpendicular to the plane, it has a width of about $15\text{-}20^{\circ}$ at half maximum, implying a cloud thickness the order of 0.4 AU. The scattering is polarized, with the electric vector parpendicular to the plane. The polarization peaks at about 20% between 50° and 80° elongation, and possibly becomes negative in the vicinity of the Gegenschein (Frey et al., 1974) due to geometric effects. The spectrum, at visual wavelengths, is a dilute solar spectrum. The close resemblance to the solar spectrum, with the lack of any blue enhancement at shorter wavelengths, seems to rule out steep size distributions, e.g. $n(a) \propto a^{-4}$, for particles in the range $1\mu < a < 10\mu$ which is most important for scattering (Frey et al., 1974), as well as contradicting models containing mostly submicron sized particles. Satellite observations over a period of 4 years have shown that any variations in intensity are less than 10%, and that no definite deviations from north-south symmetry exist (Burnett et al., 1974; Sparrow and Ney, 1972).

Spacecraft, such as the Pioneers, are also making observations in the solar system away from the earth. Soberman et al. (1974) found the zodiacal light intensity decreased as r^{-2} out to 2.25 AU, and then dropped sharply. Hanner et al. (1974) also found essentially no contribution to the zodiacal light beyond the asteroid belt.

The power-law spatial distribution used by most models,

$n(r) \propto r^{-p}$, varies widely in the value of p, from 4 (Kaiser, 1968) to 0.1 (Giese, 1973). The lower values are now more favored. Direct measurements by the Mariner and Pioneer spacecraft give a value of p = 0 near the earth (0.72 - 1.56 AU) for masses greater than 10^{-13} gm (Alexander et al., 1965; Rhee et al., 1974). Pioneer 10, with a mass limit of 2 x 10^{-9} gm, measured p = 0 from 1 to 5 AU (Humes et al., 1974), and a space density of about $10^{-15}/cm^3$. However, Hanner et al. (1974) found a drop in particle density at the 2:1 Jupiter resonance at 3.3 AU. For larger grains, the distribution may be a function of the particle size. Pioneer 10 data for grain radii in the range from 17μ to 5 x 10^4μ gives p = 3.2 for the largest and p = 1.7 for the smallest (Soberman et al., 1974). The grain concentration near the earth appears to be fairly constant, with the larger grains (a > 30μ) being much less abundant. In view of Soberman's measurement that the zodiacal light ceases beyond 2.25 AU, most of the light we see probably comes from grains within about 1 AU of the earth.

Giese et al. (1973) have calculated models for various size distributions with a spatial distribution proportional to $r^{-0.5}$, which is not too far from the spacecraft measurements. His calculations show that for $n(a) \propto a^{-2.5}$ dielectric particles have practically colorless scattering, as the observations require, whereas models with $n(a) \propto a^{-4}$ show greater overall variations from solar color, as well as

greater variations in elongation. Spacecraft measurements of the size distribution given in Leinert (1975) and reproduced here in Fig. I-1 also support a shallow size distribution for small grains, giving $n(a) \propto a^{-2.8}$ for $a < 1\mu$, $n \propto a^{-2.2}$ for $1\mu < a < 30\mu$, and $n \propto a^{-4.2}$ for $a > 30\mu$.

Models for the dust cloud have frequently assumed a lower limit to the grain size of 0.5μ, where the radiation pressure is equal to gravity for slightly absorbing dielectrics. However, small particles are continuously generated from large ones by sublimation in the outer solar corona, and driven out by radiation pressure. Grain sizes less than 0.5μ have been observed (Berg and Grun, 1973) and seem to be coming from the direction of the sun at velocities ≥ 50 km/sec. Grains this small contribute little to the optical scattering, but may be important for the thermal emission. Their infrared efficiency will be low because of their small size, but this requires them to be hotter to remain in equilibrium with the solar radiation. Their size distribution, although only slightly steeper than the intermediate sized particles, may be steep enough to allow them to contribute somewhat to the emission.

Large particles probably contribute little to the infrared emission, because of their rarity. The intermediate size range should contribute strongly to the emission at wavelengths from 8 to 14 microns. We cannot however rule out significant emission from the smallest grains.
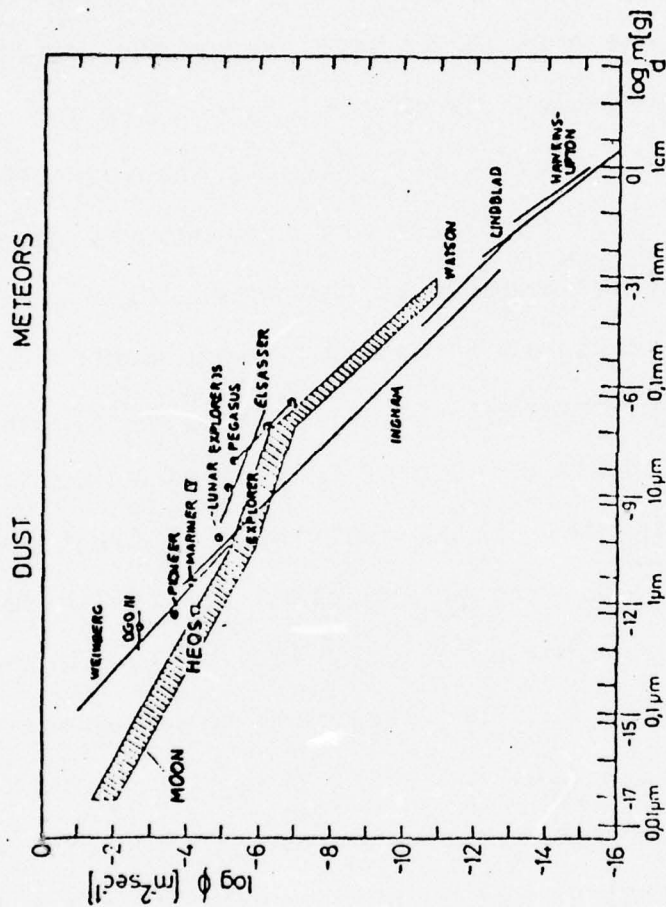
FIGURE I-1. Observed size distribution for interplane-
tary particles. (Taken from Leinert, 1975).

Since the silicate emission feature should be detectable for particles less than about 15μ in size, it should be detectable in the zodiacal dust cloud. Blackbody emission from grains with $15\mu < a < 30\mu$ will wash it out a bit, but there exists the possibility that small hot grains may enhance it. Because of the low surface brightness of the emission (6×10^{-11} watts/cm^2-sr-μ from 12-14 microns, Soifer et al., 1971) and its diffuse nature (15-20° wide), the observations must be carried out above the earth's atmosphere where a cooled telescope and absolute chopping techniques can be used.

Chapter II describes the design and calibration of the spectrometer and associated electronics constructed for these observations, as well as a description of the flight configuration. Chapter III describes the flight scan path for the observations and presents the raw data. Chapter IV contains the analysis of the data and discussion of the results. A description of the procedure used to design the telescope's diffraction baffles and to correct the data for diffracted earthlight is presented in the Appendix.

CHAPTER II

The Instrument

A. Design of the Spectrometer

The optical configuration of the spectrometer is a
2" F.L. f/3 Czerny-Turner mounting, and is detailed in Fig.
II-1. The mirrors are mounted so that their axes are
parallel. The grating is midway between them. The only
unusual feature is that the grating is mounted with its
rulings horizontal, perpendicular to the usual direction.
This puts the dispersion in the vertical plane, perpendicu-
lar to the plane of the mirrors' axes, and results in a more
compact instrument. The symmetry of this arrangement can-
cels the horizontal coma of the system. (Lindblom, 1972).
The grating itself is a 1" Bausch and Lomb aluminum grating
custom ruled to 39.37 lines/mm and blazed for 12μ. It is
located so that the secondary of the telescope is imaged on
it. A mask on the grating serves as the aperture stop.

The optical elements were located with the aid of a
ray tracing program. The program output, Fig. II-2, shows
the image of the entrance slit at the exit plane for three
wavelengths: 8, 12.5 and 16 microns. Ray bundles were
traced from the four corners and center of the slit. Each
bundle consisted of a paraxial ray and four rays spaced at
90° intervals around an f/3 cone centered on the paraxial
ray. The darkened figure at each point represents the

10

11

Entrance Slit

Grating

Detector Array

Top View

Detector Array

Side View
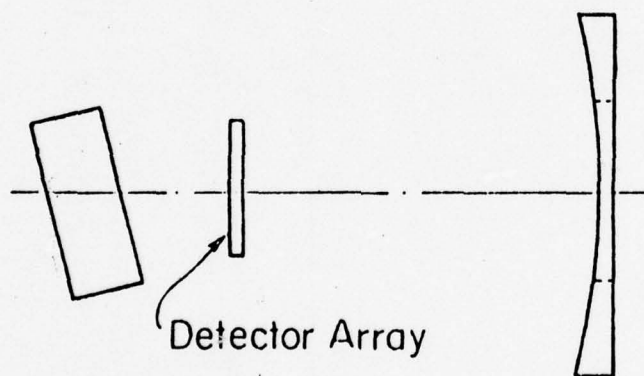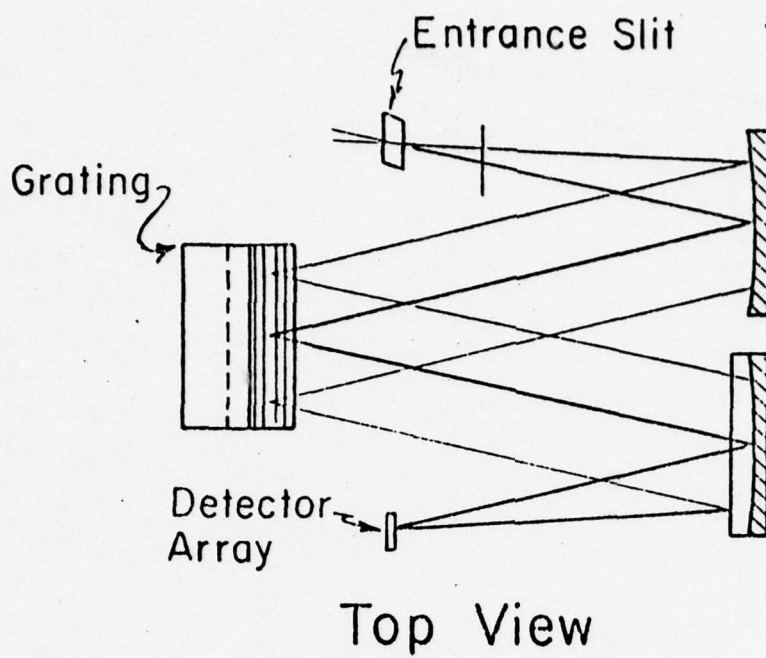
FIGURE II-1. Optical layout of the spectrometer, showing the ray paths.

Detector Array 4 x 16 mm

Image of Entrance Slit 1 x 4 mm

Geometrical Aberations Associated with
Light from the Entrance Slit
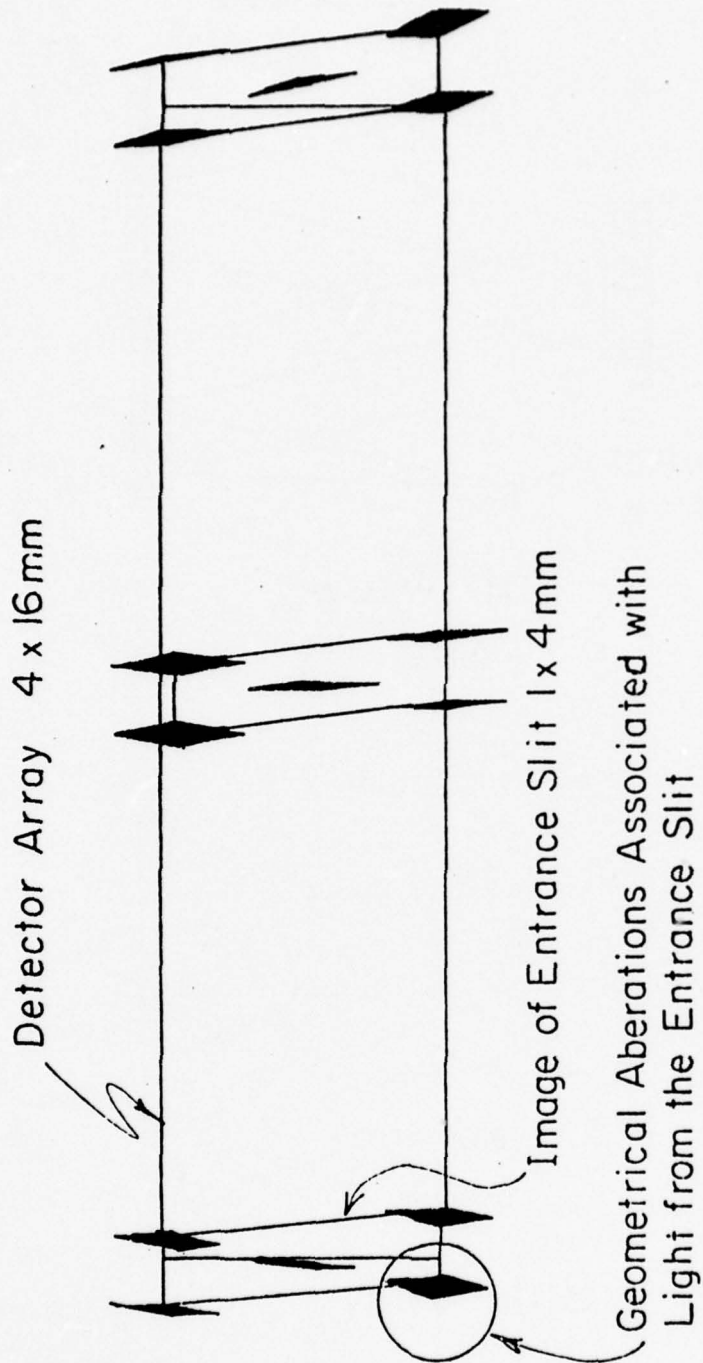
FIGURE II-2. Ray trace results for the spectrometer. The
4 x 16 mm box is the nominal array size. The
small boxes are focal plane images of the
1 x 4 mm entrance slit in 8, 12.5, and 16
micron light. The small shaded areas in the
corners of the slit images show the effects of
geometrical aberrations.

approximate outline of this cone. The large rectangle represents the nominal 16 mm x 4 mm size of the detector array. The chief ray from the center of the slit hits the collimator at an off-axis angle of 13°. This angle was the minimum needed to provide proper baffling of the system. It is large enough to cause considerable astigmatism at the exit focal plane. Because of this, the detectors were placed so the vertical astigmatic focus lies along the length of the slit, providing the sharpest spectral resolution. The horizontal focus lies about 7/32" in front of the detectors, and causes the ends of the slit image to be blurred and protrude beyond the edge of the array. This slight loss of light was not considered serious because of the diffuse nature of the expected source, the ecliptic plane.

The general principles of design, layout, and baffling were taken from James and Sternberg (1969) and Stewart (1970). The details of ray tracing are from Hopkins and Hanau (1962).

B. Construction

Both mirrors are 2" F.L. spheroids. The collimator is 1" in diameter. The focusing mirror is rectangular, 1" x 1-3/4", to accommodate the taller dispersed beam. They were specified to have the same center thickness, and to have their backs perpendicular to the optical axes to make the mounting simpler. They are held in place by aluminum brack-

ets. A thin sheet of Teflon between the brackets and the mirrors prevents chipping when they contract at low temperatures. The mirrors are thermally clamped to the holder by a thin layer of Apiezon "N"-grease.

The aperture stop was made by imaging the secondary through the collimating mirror onto a thin sheet of copper placed over the grating. The copper sheet was then trimmed to the image of the secondary. This allows only light from the secondary to pass the grating and reach the exit mirror. Light baffles were placed, using the ray trace output of Fig. II-2, to permit the detectors to see only the exit mirror. Further baffles, of aluminum sheet, were placed over the entire mirror assembly and below the collimator to prevent stray light reflecting off the dewar walls from entering the system.

The detector assembly was designed around the modified DIP package encasing the detector array. Fig. II-3 is a cross-section of the detector block. To minimize stray capacitance, the load resistors fit into the mount less than 1/4" from the detector leads. Also on the mount, close to the detectors, are MOSFET arrays used as source followers to reduce the output impedance. The filter assembly is mounted just in front of the detectors to minimize the background illumination. This assembly consists of an interference filter to block higher orders from the beam, and a BaF_2 filter to block the longer wavelengths which may reflect off the baseplate. Since the detectors are electrically

commoned to their case, the entire block assembly is insulated from the spectrometer base plate by supporting it on a thin quartz crystal.

All exposed metal surfaces were first painted with zinc chromate primer, then with a coat of 3M's "Nextel" Black Velvet. Both coats were baked on. All mating surfaces are thermally coupled with either Apiezon "N"-grease or Walther's "Goo". The entire spectrometer fits inside a 4-7/8" circle and is less than 2-1/2" high.

C. Detectors

The detector array was provided by Jim Baukus of MIT's Lincoln Labs. It is a single chip of doped silicon photoconductor. Light enters through a transparent common contact on one side. Individual contacts on the other side define the detectors, each about 4 mm x 3/4 mm. The wafer is about 0.1 mm thick, much smaller than the contact size, to minimize crosstalk between the detectors.

Two arrays were used in the testing. The first was a boron doped array. It was found to have a very low intercontact resistance, probably due to surface contamination, which caused considerable crosstalk. It was used for the wavelength calibration in a small laboratory test dewar. The crosstalk was minimized during this test by using load resistors much smaller than the intercontact resistance. An attempt was made to remove the crosstalk by etching the chip in a buffered HF solution, but it failed. As a result,
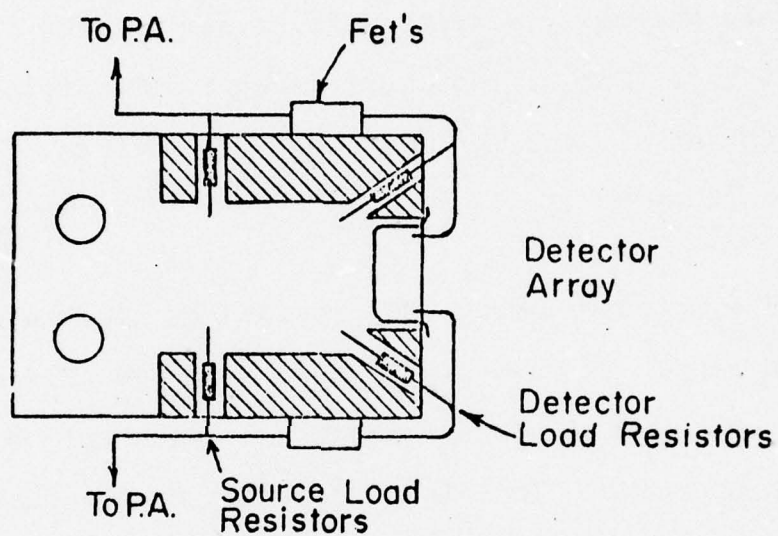
FIGURE II-3. Cross-section of the detector block, showing placement of the electrical components. The filter assembly (not shown) fits over the detector array. Light is incident from the right.

a new array of arsenic-doped silicon was obtained. This array was used for the sensitivity calibration in the flight dewar, and for the flight itself.

D. Wavelength Calibration

Wavelength calibration was done with the spectrometer mounted in a small laboratory test dewar. An auxiliary slit and diagonal were mounted to put the beam in the proper direction. The test was done using the first boron-doped detector array. The FET's were not used, and the load resistors were located outside the dewar.

A Perkin-Elmer Dual-Beam IR Spectrophotometer, converted to f/3 operation, was used as a monochromator. While it automatically scanned in wavenumber, the output of one detector was amplified, synchronously demodulated, and recorded on a strip chart. This was repeated for all detectors. Finally a reference spectrum was taken with the monochromator output falling on a thermocouple thru a piece of polyethelene from which the dewar window had been cut. This established the power spectrum at the entrance slit. The wavelength response was calculated by dividing the individual detector runs by this reference spectrum. The results are shown in Fig. II-4.

The reference spectrum showed the polyethelene window to be opaque in the wavelength region corresponding to detectors 15 and 16. Since the window is not used in the flight optics, the center wavelengths for these detectors

18
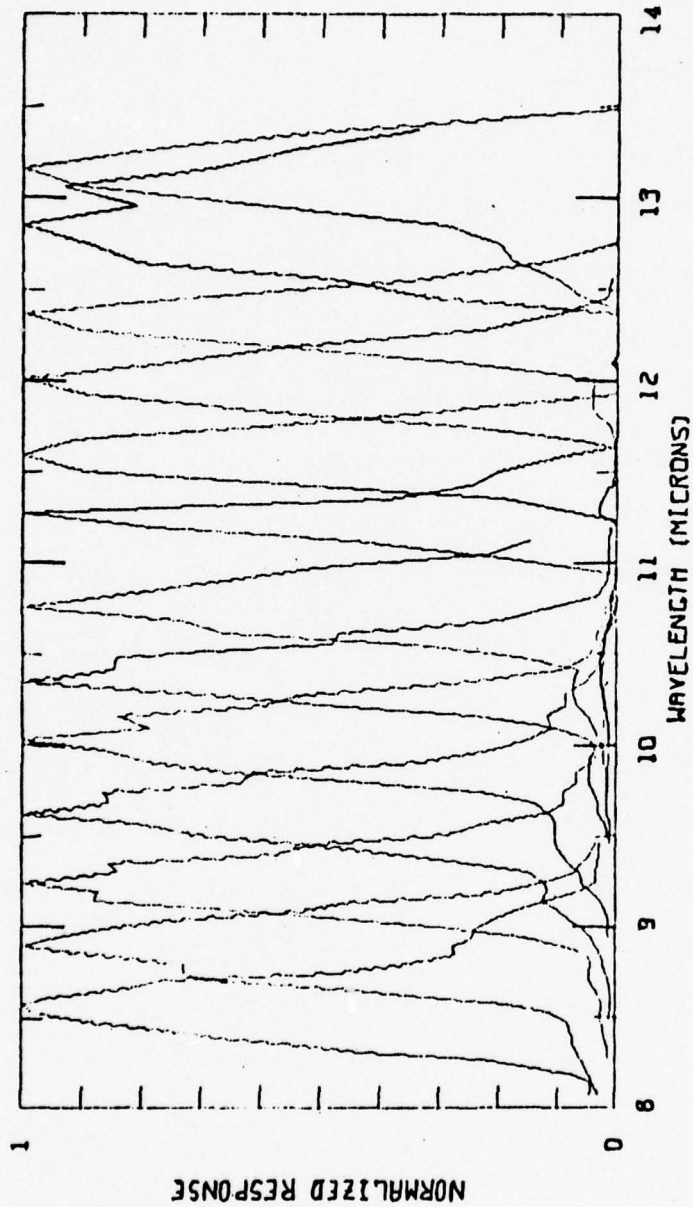
FIGURE II-4. Wavelength response of the detector array, normalized to unity at the peak. Detectors 14-16 are not shown because they were affected by the opacity of the dewar window.

TABLE II-1

Wavelength Calibration of the detectors.

Observed vs. Calculated Values.

Detector	λ_c (μ) Measured	λ_c (μ) Calculated	$\Delta\lambda$ (μ) Measured	$\Delta\lambda$ (μ) Calculated
1	8.59	8.57	0.39	0.377
2	8.95	8.95	0.36	0.378
3	9.28	9.33	0.51	0.378
4	9.72	9.70	0.40	0.379
5	10.08	10.08	0.34	0.379
6	10.46	10.46	0.44	0.379
7	10.82	10.84	0.36	0.378
8	11.19	11.22	0.27	0.377
9	11.65	11.59	0.31	0.376
10	12.01	11.97	0.37	0.375
11	12.37	12.34	0.35	0.373
.12	12.72	12.72	0.37	0.371
13	12.99	13.09	0.57	0.369
14	13.48	13.45	0.29	0.367
15	-----	13.82	----	0.364
16	(14.57)	14.18	(0.31)	0.361

had to be taken from the ray trace. Since the physical size of the detectors was not accurately known, it was used as a parameter in the raytrace. The best agreement was found for a detector width of 0.814 mm. Inspection of the array showed the width to be the order of 3/4 mm, but no attempt was made to get too close to the array for fear of damaging the delicate wiring of the contacts. Table II-1 lists the observed center wavelengths of the individual detectors against the calculated ones. The agreement is excellent, and gives a degree of confidence to the calculated center wavelengths for detectors 15 and 16. The large disagreement on detector 16 is due to two effects: the opacity of the window at the calculated center wavelength, and the large crosstalk exhibited by this array. Essentially, #16 is responding to light falling on the end of the chip beyond the last contact, i.e. on "detector" 17. The agreement on the rest also shows that they are well determined in spite of the crosstalk.

In contrast, I have little faith in the measured bandwidths as they are much more sensitive to the crosstalk than the peak response. A simple model of the crosstalk is to assume that it is due to a resistor between the contacts. For the case of two detectors, only one of which is illuminated, this model predicts a spurious response at the dark detector proportional to the load resistance divided by the intercontact resistance. The smallest load resistor consis-

tent with good signal-to-noise (15K) was used for calibration. If the intercontact resistance, i.e. the contamination, varies along the chip from one detector to the next, this will have a direct effect on the measured bandwidth. Table II-1 also lists the observed bandwidths, taken as full width at half maximum, against the calculated ones. The measured values often differ significantly. I take the calculated ones to be correct for the flight detectors, since they showed little crosstalk.

E. Electronics

The post-detector electronics consists of four sections: MOSFET impedance converters in the dewar, preamplifiers, synchronous demodulators (SD's), and breakpoint amplifiers. In addition, there is a provision for periodically shorting the inputs to the SD's to measure any DC drift. Following the electronics is a commutator that samples each output 10 times a second for telemetry on a single channel to the ground station.

Impedance Converters

The MOSFET's used in the dewar are Siliconix G118AL's. These are available in flat pack arrays of 6 FET's each. All the gate leads are on one side, and their spacing is the order of the detector lead spacing, which enables a compact mounting arrangement. Four such chips are used, providing 8 spare FET's. The gate capacitance of these FET's to the source and drain totals about 6 pf. This limits
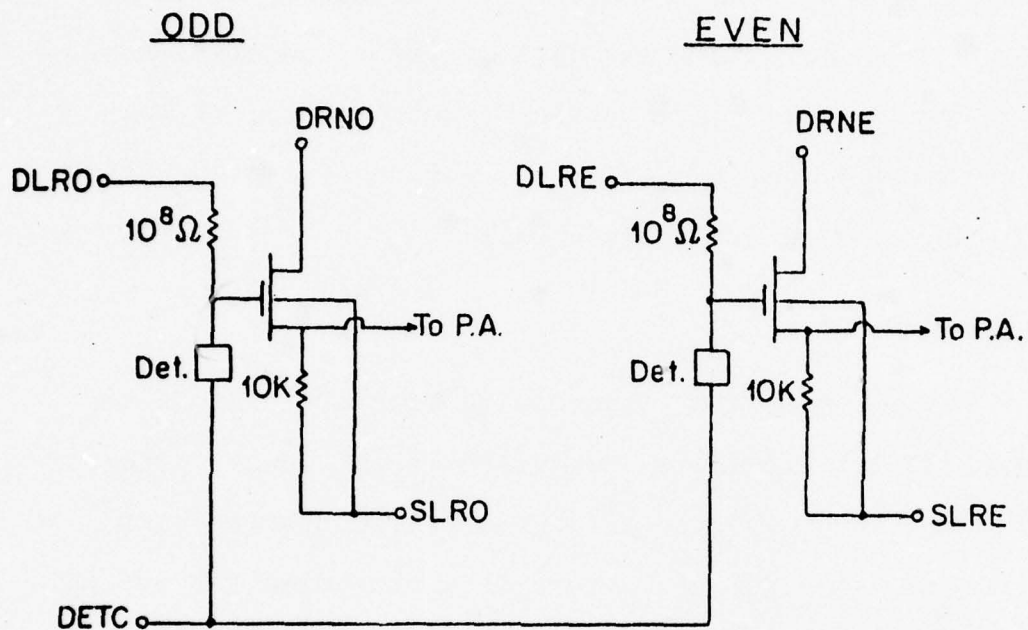
FIGURE II-5.   Schematic of the dewar circuits.
The detector load resistors, source
load resistors, and drain leads
for the odd and even detectors were
brought out of the dewar separately
to minimize crosstalk.

the maximum detector load resistor to about 10^8 ohms for
150 Hz chopping. A schematic of the dewar circuits is shown
in Fig. II-5. The noise at the source lead was measured to
be about 175 nV/$\sqrt{}$Hz. It is attributed to the Johnson noise
of the load resistor, which should be 145 nV/$\sqrt{}$Hz after
attenuation by the RC at the gate, and about 100 nV/$\sqrt{}$Hz
due to the FET and/or the detector.

Preamplifiers

LM308's were chosen for the preamps because of their
high rejection of power supply noise (> 80 db), and their
low input noise voltage (~ 50 nV/$\sqrt{}$Hz), which is smaller than
the noise at the FET's. They also require very little power
which is important because the entire electrical system of
the rocket runs off batteries. The circuit is AC coupled to
the signal and provides a nominal gain of 101. Following
the preamps is a set of resistors and capacitors connected
to a relay which is used to short the AC output for one
second every minute. Resistor R_1 (Fig. II-6) protects the
preamps from this shorting, and, with the following resistor
and capacitor, lowers the overall gain. All 16 preamps
used for the flight, and 8 spares, were calibrated and
agreed to within 1% with a net gain of 90.6.

Synchronous Demodulators

Following Fig. II-7, the AC coupled input from the
preamps goes first into an amplifier, then through a unity
gain inverter. This provides two signals, 180° out of phase
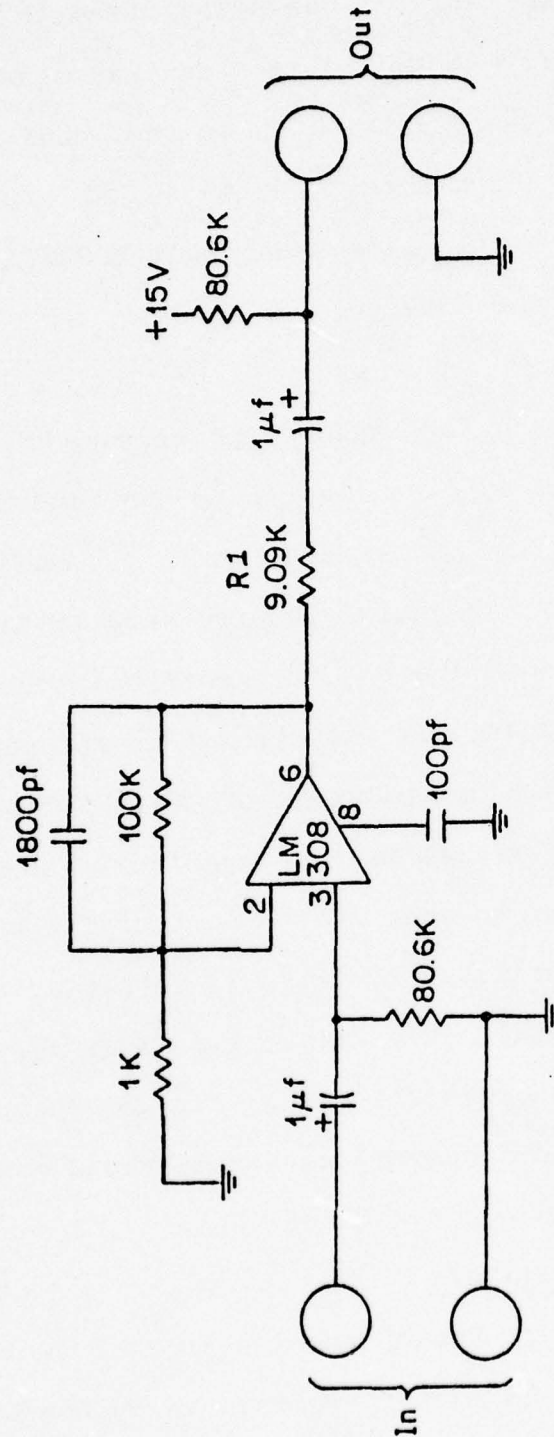
24

FIGURE II-6. Schematic of the preamplifier circuit. The output is connected to a relay that shorts the AC output periodically. Resistor R_1 protects the preamp from the shorting.
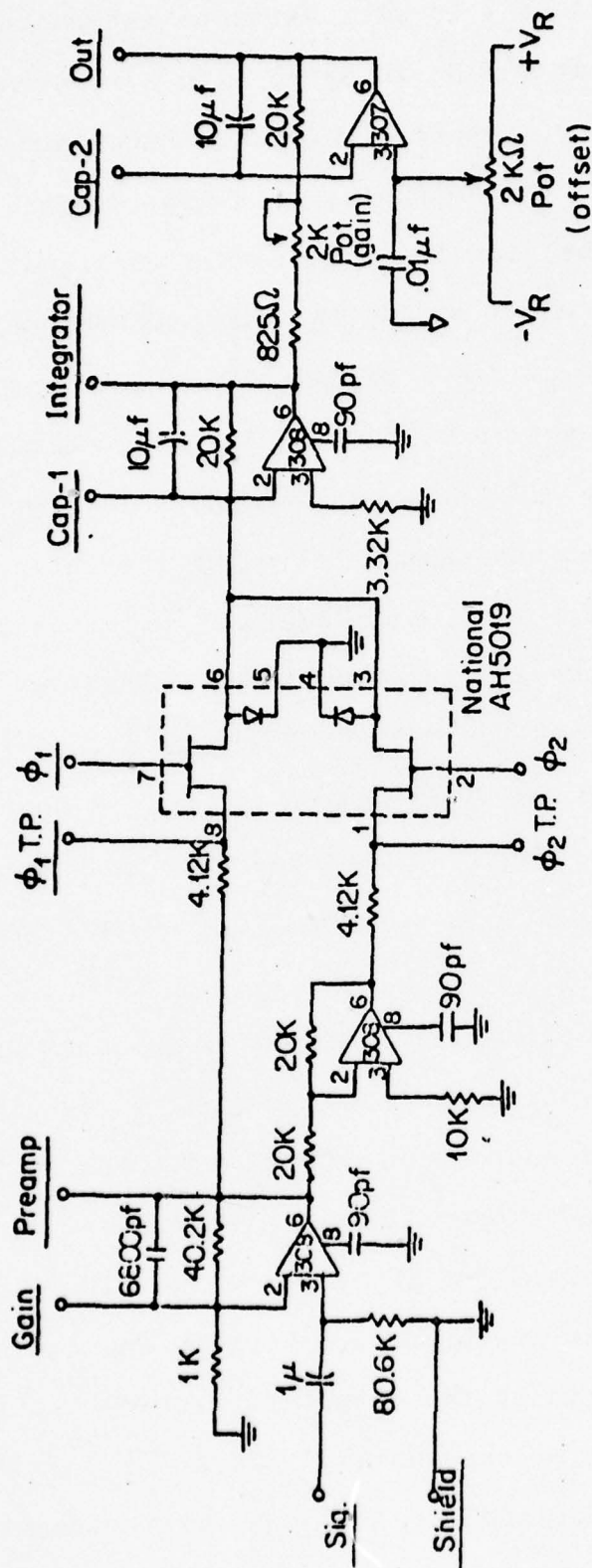
FIGURE II-7. Schematic for the synchronous demodulator circuits. See text for explanation.

with each other. A pair of JFET switches alternates between these two signals at 150 Hz in synch with a reference signal derived from the chopper. When this reference signal is properly phased, the switching will provide full wave rectification of the signal. This rectified signal is fed into an integrator whose output is then proportional to the AC amplitude of the original signal. The time constant of the integrator was set to 0.2 sec. Since the commutator samples each channel 10 times per second, this provides two samples per time constant. Following the integrator is an output amplifier. Two potentiometers on this allow variations in the overall gain and the DC offset of the output. The gain was set so that an AC signal of 2mV rms at the input gives a 5V DC shift at the output. A capacitor in the feedback loop provides a second pole to the filter, further reducing the 300 Hz component of the integrator output.

The reference signal is obtained from the chopper driver. It is fed into a phase shifter, Fig. II-8, consisting of two one-shots and output amplifiers to drive the JFET switches. All the SD's operate at the same phase.

LM 308's were used for the first three stages of the SD's because of their low power consumption and low noise. An LM 307 was required at the output to provide sufficient current to drive the breakpoint amplifiers.

The SD's are designed so that the first element to saturate is the output amplifier. Calibration showed them
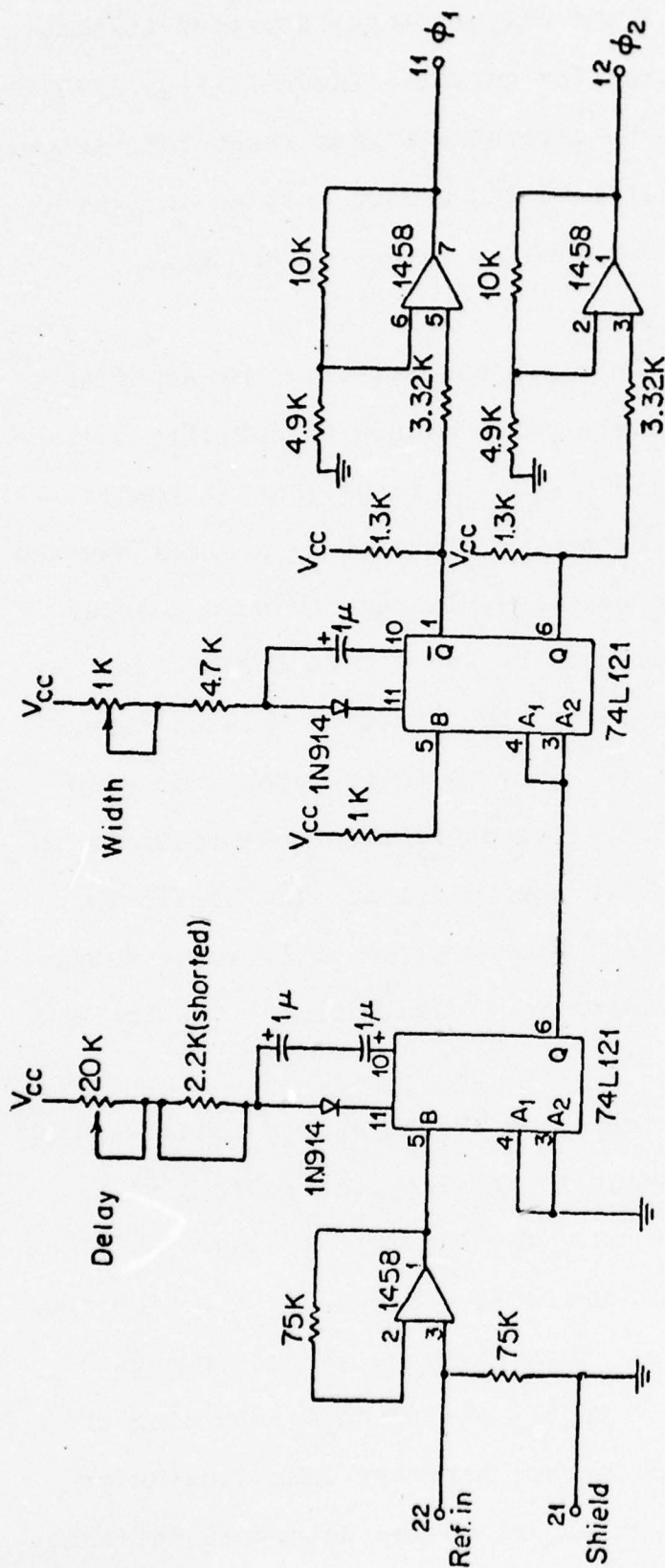
FIGURE II-8. Schematic for the phase shifter. The input is a reference frequency derived from the chopper. The output amplifiers drive the JFET switches in the SD's.

to be very linear until the output stage saturates at about 14 volts. A typical transfer curve is shown in Fig. II-9. The SD's were found to be very stable with respect to temperature variations. Cooling to 0°C caused only an insignificant change in the offset, and no change in the gain.

Breakpoint Amplifiers

Breakpoint amplifiers are piecewise linear amplifiers exhibiting relatively sharp gain changes at specific output voltages. The circuit, Fig. II-10, shows that at low input voltages, the gain switching transistors are off and the gain should be 10. In practice, leakage through the low gain transistors reduces this by about a factor of two. At output voltages above 2 volts, the first transistor turns on, cutting the gain to 1. Above 4 volts output the gain is further reduced to 0.1. Telemetry requirements limit permissible signals to less than 5 volts. The breakpoint amplifiers extend this range to cover up to 10 volts output at the SD's, while providing good resolution at the low end.

Noise

If the 175 nV/$\sqrt{\text{Hz}}$ observed at the source leads were directly amplified, without integration, it would give 154 mV/$\sqrt{\text{Hz}}$ at the SD output. The electrical bandwidth of a two pole filter is 1/8RC, where RC = 0.2 sec + the time constant of the integrators. This gives 24 mV rms or about 122 mV PTP noise at the output. Strip chart recording of the SD output taken with the spectrometer operating under low background and with no signal on the detectors confirmed
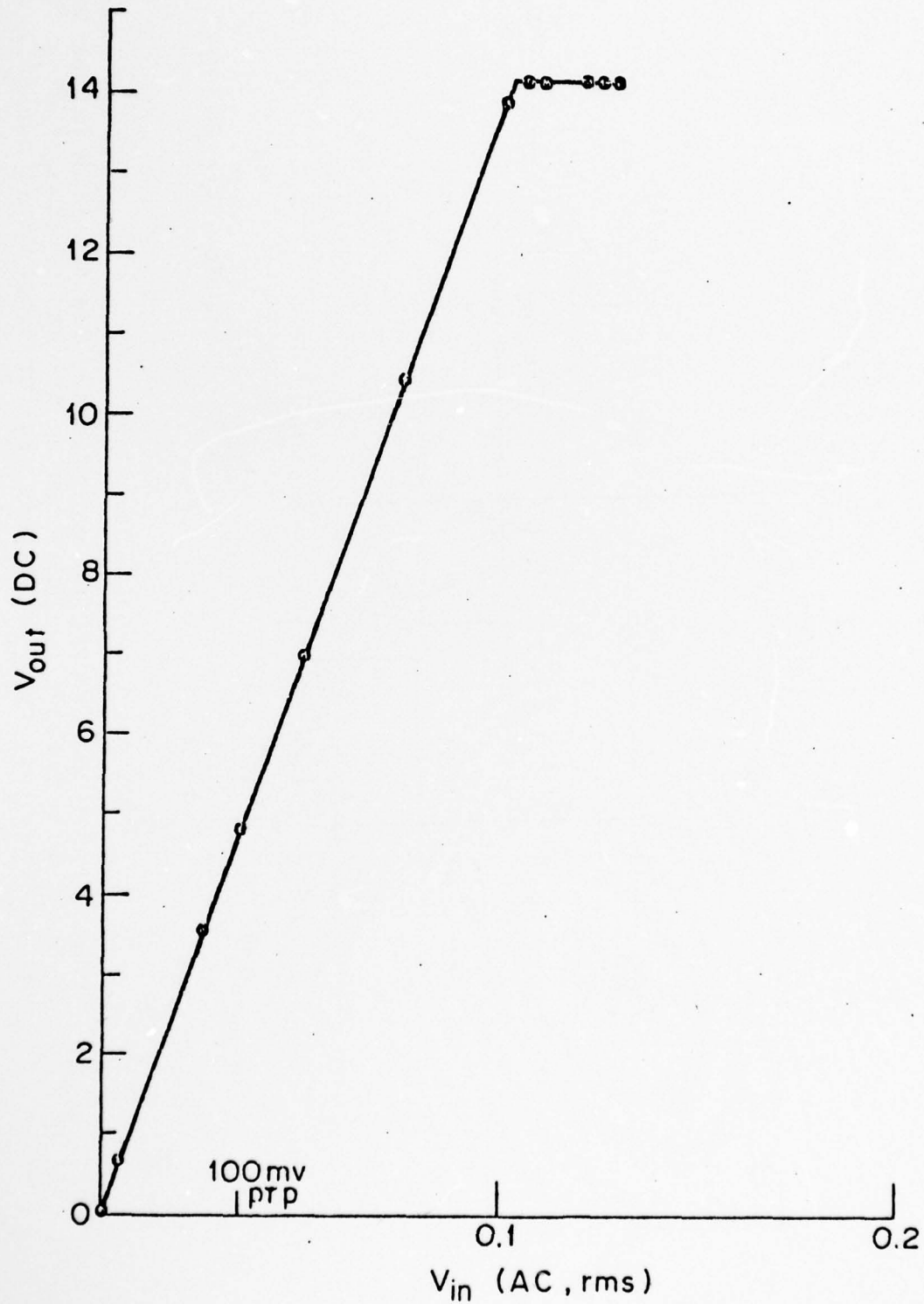
FIGURE II-9.   Typical transfer curve for the SD's.   DC output
vs. AC input for in-phase signals.
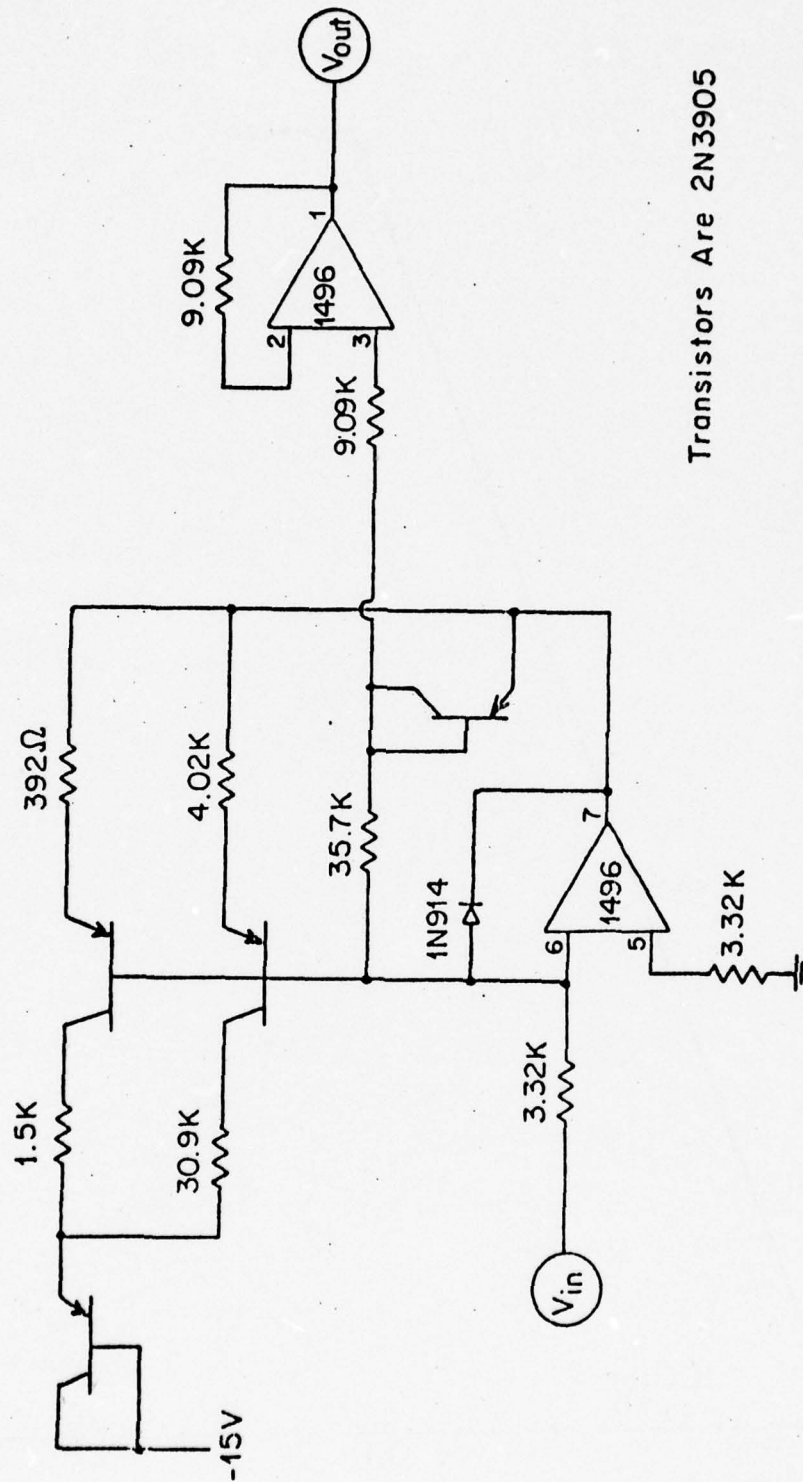
Transistors Are 2N3905

FIGURE II-1C. Schematic for the breakpoint amplifiers. The two transistors in the feedback loop provide grain switching at output voltages of 2 and 4 volts. The other two transistors are for temperature stability.

this, showing that the limiting noise of the entire system
is generated by the load resistor and FET. Shorting the
preamp input reduces the output noise significantly. The
noise level is thus proportional to the gain of the SD's.
This gain was chosen to make the output noise greater than
the telemetry noise which, because of bandwidth limitations
and the commutator rate, is the order of 100 mV.

F.   The Flight Configuration

Figure II-11 is a drawing of the assembled flight
dewar and optics. The entire optical system, telescope and
spectrometers, was cooled to cryogenic temperatures,
$T \leqslant 10^{o}K$, by placing it in a cavity in a liquid helium
dewar. This reduces the background radiation and makes
the detectors more sensitive.

The Cassegrain telescope optics were designed by Dr.
Judith Pipher to minimize spherical aberration over the
field of view. A diagram of the telescope is shown in Fig.
II-12. Table II-2 contains the optical parameters. The pri-
mary is 7.5" in diameter and the telescope operates at $f/3$,
matching the spectrometers. On the primary mirror's back
plate the entrance apertures, chopper, beam splitter, and
spectrometers are mounted. A second spectrometer, similar
in design to the one already discussed but with a different
grating and detector system, covering the region from 30 to
120 microns, was also mounted on the back plate. The results
from this spectrometer will be discussed by Pipher (1976).
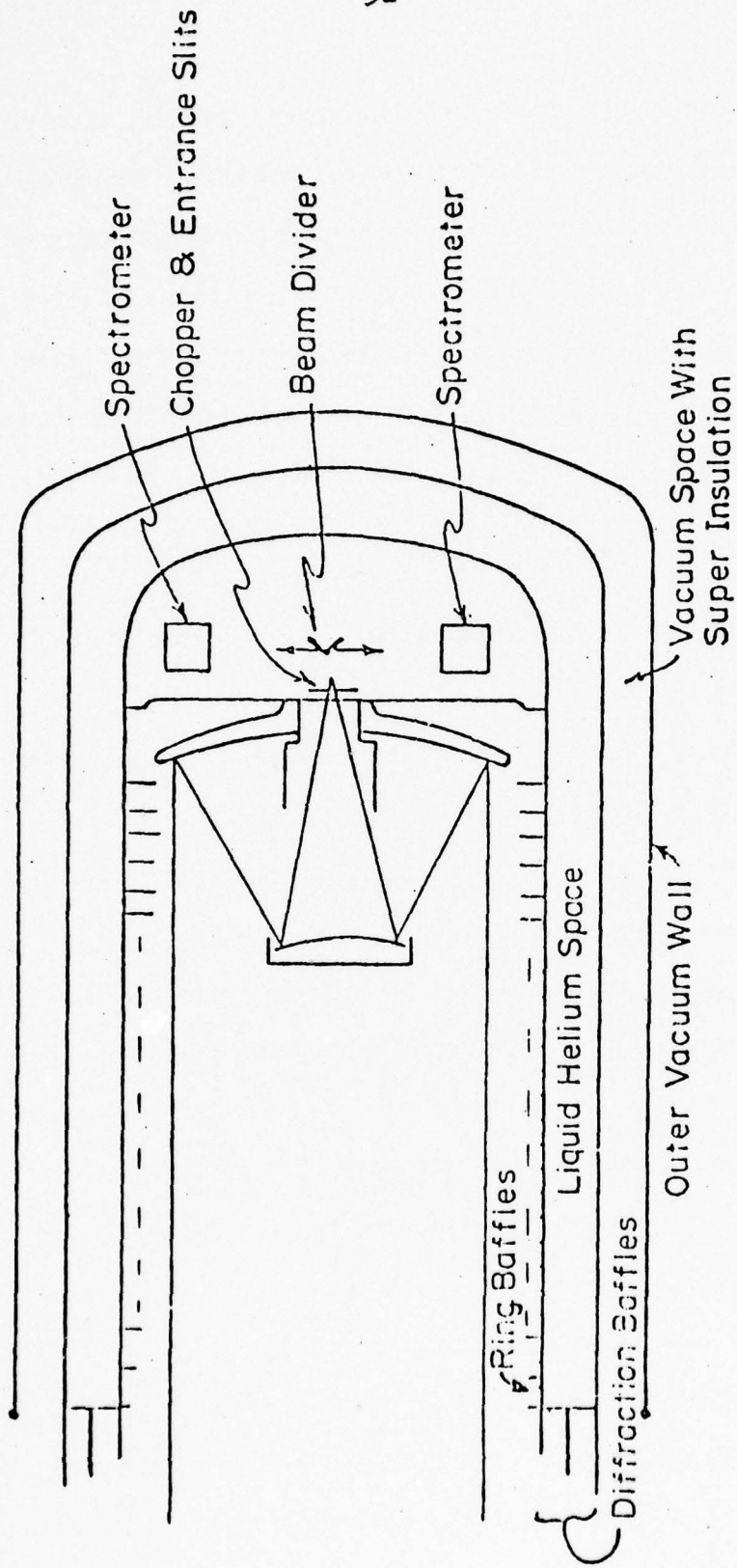
FIGURE II-11. Assembly drawing of the flight dewar, showing positions of the telescope, spectrometers, and baffles.
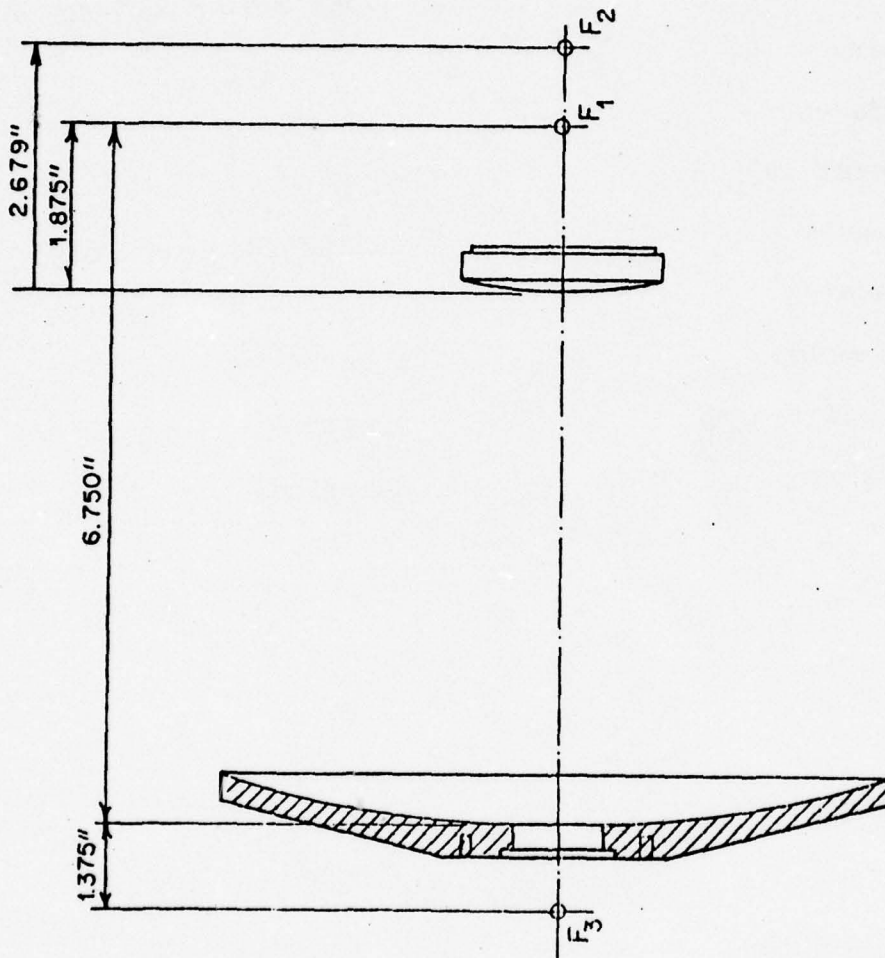
FIGURE II-12. Drawing of the Telescope Optics. F_1, F_2, and F_3 are the focal points of the primary, secondary, and telescope respectively.

TABLE II-2

Optical Parameters of the Telescope

Configuration	Dahl-Kirkham
f/	3
$A\Omega$	6.353×10^{-3} cm^2-sr
Primary	
Diameter	7.5"
Focal Length	6.75"
Figure	Ellipsoid, e = 0.8193
Secondary	
Diameter	2.25"
Focal Length	2.679"
Figure	Spherical

The two spectrometers use different entrance apertures and electronics, and they are independent. The entire telescope/spectrometer assembly can be aligned outside the dewar and inserted as a unit.

Above the telescope, along the inner dewar wall, is a set of reflection baffles to help eliminate stray light striking the inner dewar wall. At the front of the dewar are three cylindrical diffraction baffles designed to minimize the amount of earth light diffracted past the ends of the tube (see the Appendix). The baffle surfaces, with the exception of the outer diffraction baffle, were roughened and blackened by a coat of 3M's Black Velvet thinned in butanol and mixed with #180 silicon carbide grit, all painted over a zinc chromate primer. The procedure that seemed to work best was to first spray a coat of paint over a small area. The grit was poured on the wet surface, which was then tilted and shaken to give an even layer of grit. Excess grit was removed. When the entire surface was treated in this way, a final coat of Black Velvet was applied and the result baked dry in an oven.

G. Sensitivity Calibration

The sensitivity of a detector to radiation is a function of the radiation's intensity. Under high background conditions, i.e. when the radiation is intense, the sensitivity is typically lower and the detector noise higher. The motivation behind cooling the entire optical system to

cryogenic temperatures is primarily to reduce the background intensity. Since the detectors operate under low background conditions during the flight, it is necessary to calibrate them under similar conditions. The calibration blackbody must be located inside the dewar and the dewar must be sealed so no stray light can enter.

Pre-flight Calibration

Early attempts to use the liquid nitrogen blackbody constructed for previous rocket flights (Soifer, 1972) were not successful. A $77^{\circ}K$ blackbody spectrum is too steep in the 8-14 micron region to allow calibration of the shorter wavelength detectors. These tests did point out a long wavelength light leak, however, and resulted in a second filter of BaF_2 being placed over the detectors. They also showed a short wavelength leak in the blackbody.

A new blackbody was constructed to produce warmer spectra without producing so much intensity it overloaded the detectors. It is shown in Fig. II-13. It consists of a heating resistor and temperature sensor. The temperature sensor is a TI "Sensistor", and is estimated to be accurate to $\pm 2^{\circ}K$ for temperatures above $80^{\circ}K$. The resistors were thermally coupled with GE varnish and wrapped in aluminum foil, which was then painted black. This was suspended inside a shiny cavity by a stainless steel wire. The wire serves as a heat sink. The cavity aperture was a 0.32 mm diameter hole cut in shim stock. The entire assembly was

mounted on the inner dewar lid. Measurements of the lid and cavity temperatures showed that they remained below about 15°K throughout the calibration runs. They do not contribute any significant radiation.

The aperture had to be kept small to keep the total radiated power down. Since the projected diameter of a f/3 cone at the top lid is about 6", the blackbody only illuminates a fraction of the beam. Several runs were made with it in different portions of the beam, which showed that the beam was not uniform. With the telescope optics removed and the blackbody on the optical axis, the response of the detectors was about a factor of two higher than with it located 2-1/8" off axis, the radius that includes half the area of the beam on the top lid. This made calibration more difficult.

The procedure used to calculate an average sensitivity over the beam was as follows. Calibrations performed with the blackbody in the same position were averaged together in the usual manner. For each detector, this gives a sensitivity for that portion of the beam illuminated by the blackbody. The average of these values is the mean response of all detectors for that part of the beam. The ratio of the individual detector sensitivites to the mean response gives the sensitivity profile as a function of wavelength. This is assumed to be independent of the portion of the beam illuminated. The profiles for all the blackbody positions

are then averaged together for each detector and the result multiplied by the average of the mean responses. This gives the sensitivity for each detector averaged over the beam. The results of this procedure for the three runs conducted at White Sands just prior to the flight are given in Table II-3.

Test results for several runs with the blackbody in the same position showed a slow degradation of sensitivity in some detectors. Occasionally this was followed by a sharp drop of a factor of 3 or more. This was traced to the FET impedance converters in the dewar. When a detector was connected to an adjacent FET on the same chip the nominal sensitivity was usually restored. The cause of this effect is unknown. It may be due to the cumulative effects of thermal shock during cooling, or perhaps to mistreatment of the FET's between runs, although they were handled carefully and their gates were protected by diodes. This adds a degree of uncertainty to the calibrations beyond what the random errors would indicate, although the slow degradation in performance before a FET dies completely usually amounts to less than a 10% effect. Nevertheless, only the calibrations performed in the field, within a few days before the flight, were used, to be on the safe side.

Two detectors deserve special mention. The contact on detector #14 was found to be open prior to the first cooldown in the flight dewar. Lacking the proper equipment to repair the contact, this detector was not used. A signal
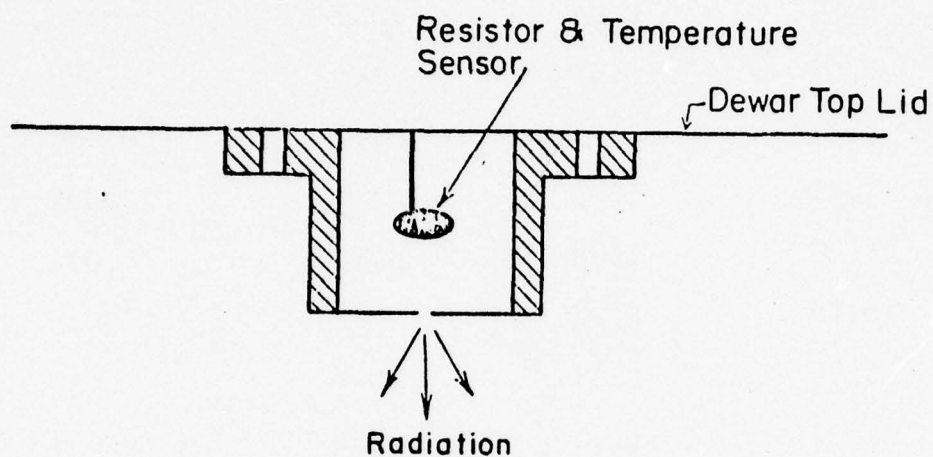
FIGURE II-13. Drawing of the blackbody used for the
pre-flight calibrations. The aper-
ture size is 0.32 mm. The horizontal
line at the top is the dewar's top
lid, which fits over the innermost
diffraction baffle.

TABLE II-3

Detector sensitivities, results of the pre-flight calibration. Sensitivity units are 10^{-10} watts/cm^2-sr-μ per Volt.

Det.	$\lambda(\mu)$	Sensitivity	RMS Error	Fractional Error
1	8.57	2.84	.272	.096
2	8.95	2.57	.227	.088
3	9.33	2.43	.194	.080
4	9.70	1.73	.036	.021
5	10.08	1.69	.037	.022
6	10.46	1.26	.029	.023
7	10.84	1.43	.049	.034
8	11.22	1.30	.050	.038
9	11.59	1.21	.041	.034
10	11.92	1.47	.146	.099
11	12.34	1.84	.190	.103
12	12.72	.710	.052	.074
13	13.09	8.45	3.76	.445
14				
15	13.82	.758	.054	.072
16	14.18	.809	.057	.071

consisting of the average of the other detectors was placed on the data channel previously assigned to #14. The other detector, #13, shows a much lower sensitivity than the other detectors in Table II-3. This normally would indicate a FET failure as discussed above. However, connecting #13 to other FET's did not cure the problem as it had for other detectors in the past. During the flight, #13 seemed to perform much better than the pre-flight calibrations would indicate (see Chapter IV). Consequently, I have little faith in its calibration, and do not trust the corresponding signal levels it implies.

Post-flight Calibrations

Calibrations were also made after the flight to check the performance of the spectrometers against the pre-flight calibrations. Because of technical problems, the post-flight calibrations were more difficult and not entirely successful.

In order to measure the beam averaged sensitivity of the spectrometer directly, a new blackbody was constructed for this calibration. It is similar to the pre-flight one, but larger, with 8 holes in the cavity placed to cover equal areas of the annular f/3 beam. To ensure equal temperature radiation at all the exit holes, the blackbody had to be small. The telescope was removed and the blackbody was mounted on the secondary tripod to provide uniform coverage of the beam. Because of the increased number of holes and the reduced distance between the blackbody and the entrance

slit, lower temperatures, $\sim 100\text{-}120^\circ$K, had to be used to keep the power level down. This made calibration of the short wavelength detectors difficult. If the temperature was raised high enough to see a reasonable signal on detector #1, the thermal load of the blackbody would heat up the mirror plate. This did not matter much since some of the short wavelength detectors could not be made to work.

Detectors #3 and #4 showed no response to any radiation levels. Detector #13's output was pinned at +15 volts. (During the flight, #3 and #4 behaved normally, although #13 appeared to be more sensitive than during the pre-flight calibration). For the second post-flight run, the FET's on these detectors were changed, and, during the run, the cards with their electronics were exchanged with cards from working channels. Nothing helped, and the channels remained dead. I emphasize that these detectors did not behave this way during flight, and can only conjecture that something happened to them, either upon impact with the desert after the flight, or during shipment home to Cornell. Possibly the contacts opened up, as #14 had done earlier, or the load resistors cracked.

In spite of these, and other problems, five detectors gave reliable readings in the first run and all but the above three worked in the second run. The five that worked during the first run agreed with the pre-flight calibration to better than 10%. For the second run, the spectral profile

of the sensitivity curve was similar to the pre-flight, but the overall sensitivity level was about 15% more sensitive. This may be due to the fact that the detector block was about 0.5°K warmer during this run than in previous runs. The net result of the two runs confirms that the beam averaging technique used in the pre-flight calibration was accurate.

CHAPTER III

The Flight

A. The Scan Path and the Aspect Solution

The payload was launched on October 14, 1975 at
4:30:0.755 MDT aboard an Astrobee F from White Sands Missile Range, N.M. When the powered flight was over and the
Attitude Control System and yo-yo despin mechanism had stabilized the fast roll used during the ascent, the ACS began the nominal scan pattern. The rocket was rolled to put
the pitch axis at the azimuth of the ecliptic pole, and
yawed down to put the pitch axis at the pole and the roll
axis (equal to the optical axis) on the ecliptic plane.
A fast pitch maneuver 60° east brought it to the beginning
point where the nose cone was ejected. Subsequent maneuvers
consisted of a constant pitch rate westward along the ecliptic plane at $1/3^{\circ}$ per second, combined with up and down yaw
dithers between ecliptic latitudes of $+30^{\circ}$ to -30° at a
rate of $2^{\circ}/sec$. The fast scans in latitude, combined with
the slow scan along the plane provided a crossing of the
ecliptic every 30 seconds, at elongation increments of 10°.

An onboard aspect camera and flapper system recorded
interrupted star trails crossing within 27° of the field of
view as the rocket scanned. This was to record any deviations of the actual scan path from the nominal one. Unfortunately, the scan rate was too fast to permit stars fainter

44

than about 3rd magnitude to be recorded. Thus a complete scan path reconstruction was not possible. However, enough aspect positions over a sufficient time span were available to indicate that the actual path differed by less than about a degree from the nominal path. A plot of the aspect solution in geocentric ecliptic coordinates is presented in Fig. III-1. Using this solution, however, the peak ecliptic signals were consistently observed at an apparent latitude of about $+5^\circ$. The solution may not be as accurate as the pictures would indicate, but it is good enough to tell us approximately where the ecliptic plane is, and that is all that is required.

B. Problems During the Flight

At tip eject, all channels saturated due to the radiation from the hot nose cone. This verified that all detectors and electronics were working. As the nose cone drifted out of the field of view, the signal level dropped slowly. By the end of scan 2 it provided essentially no contribution to the raw signal.

After the beginning of scan 4, the signals began to rise, and after about T+180 seconds, in scan 5, began to show large, rapid fluctuations. Both spectrometers saw it, so the source is probably external to the payload. The rapid fluctuations are probably due to rotating small particles blown out of the motor section. The sustainer engine sepa-
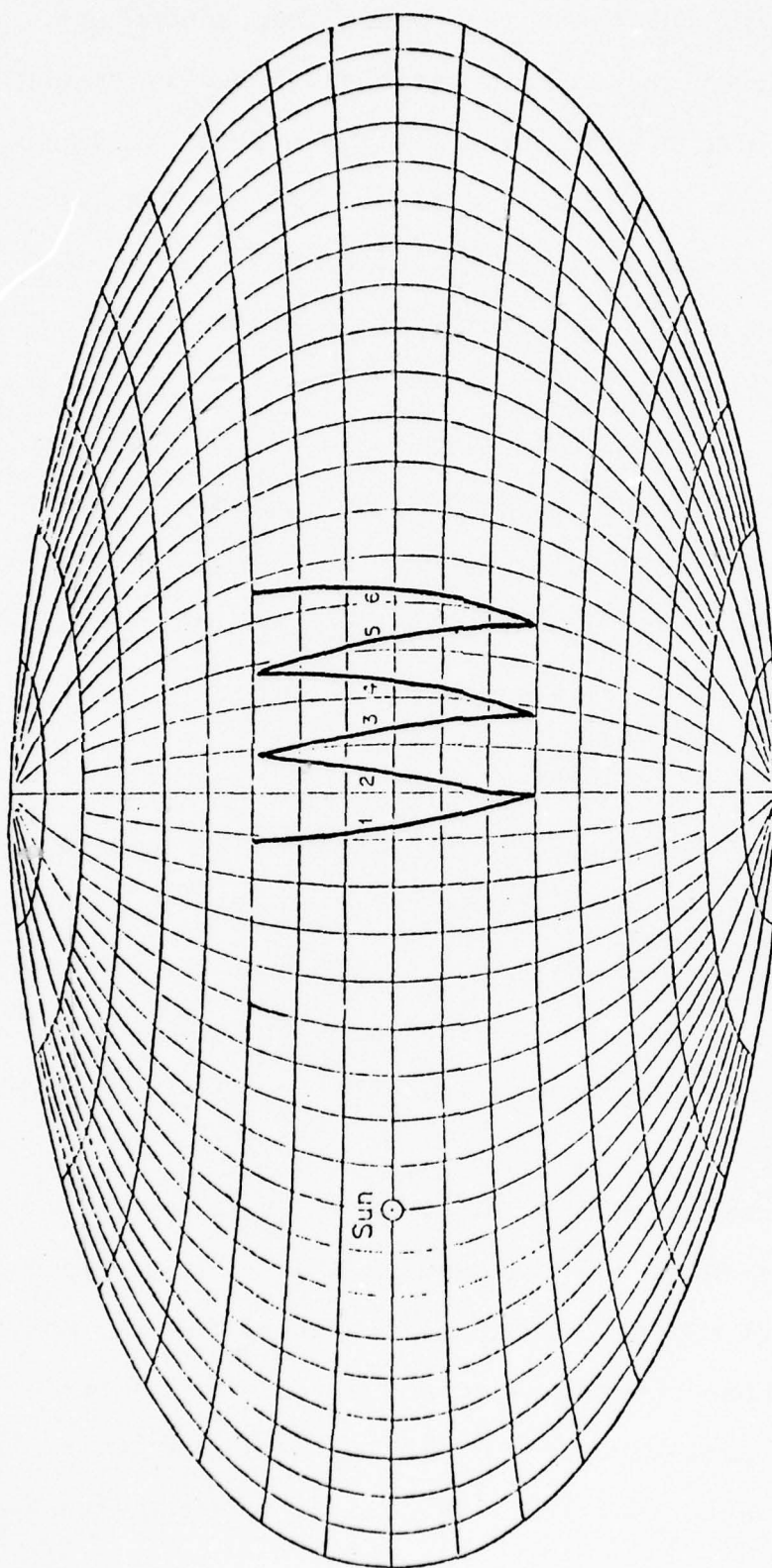
FIGURE III-1. Scan path for the observations in geocentric ecliptic coordinates. The sun is shown on the ecliptic plane at zero elongation. Scan 3 occurs between latitudes of +30 and -30° at elongations from ~ 99 to 108°.

rates from the payload after powered ascent, but remains in
a similar ballistic trajectory. If it began to tumble, it
could direct a weak residual exhaust from unburned propel-
lant lining the walls of the fuel cavity towards the pay-
load. Data beyond the beginning of scan 4 is contaminated
by this and probably unusable.

C. The Raw Data

The raw data levels, in volts, for the broadband
sum channel covering the first 5 scans are presented in Fig.
III-2a-2e. The gaps in scans 2 and 4 that occur near the
ecliptic crossings are the result of SD shorts caused by
an onboard timer every 60 seconds. Where these shorts occur
is a matter of chance, depending on the time it takes to
stabilize the rocket's fast roll after powered ascent. It
is unfortunate that they occurred just at the ecliptic
crossings. A more mystical person than I might see some
significance in this. The smooth curve below the data is
the earthshine level, calculated by the procedure des-
cribed in the Appendix.

Scans 1-3 clearly show increased signals in the
vicinity of the ecliptic plane. The excess signal early in
scan 1, at high ecliptic latitudes, is due to the nose
cone drifting out of the field of view. In scan 2, an
SD short occurred just during the ecliptic crossing. Scan
3 shows a clear ecliptic signal, with relatively little
outside contamination, and contains the only useable data.

From the end of scan 3 onwards, the general signal level
rises. By scan 5 it begins to show rapid fluctuations,
attributed to residual sustainer exhaust as mentioned above.
The generally higher signal levels are attributed to the
sustainer itself, just out of the field of view. This inter-
pretation of events is strengthened by the spectrum observed
during scan 4, which shows the λ^{-4} dependence indicative of
a hot blackbody.

First observations from new experiments are generally
plagued by technical difficulties. This flight is no ex-
ception. Only about 10% of the data, i.e. scan 3, is usable
with any degree of confidence. The data analysis in the
next chapter is restricted to scan 3.
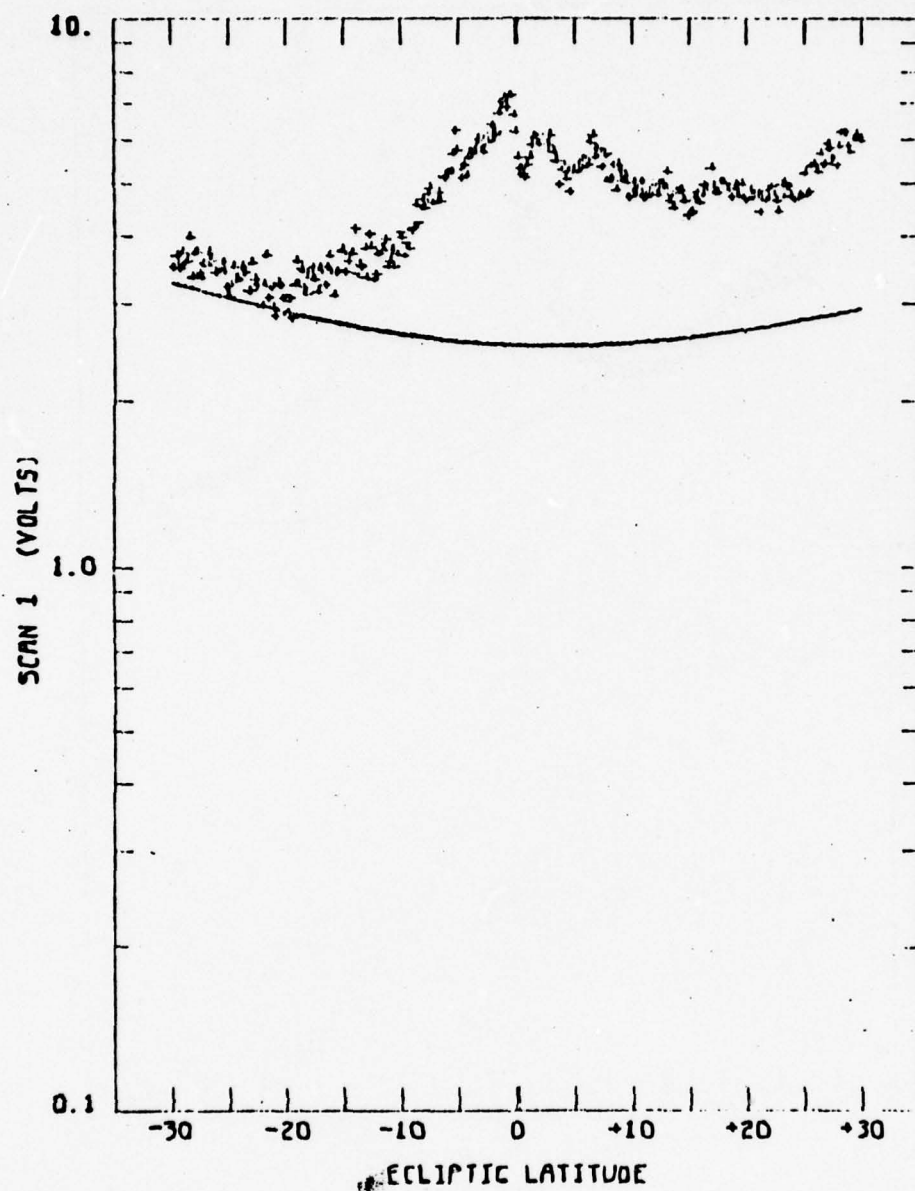
FIGURE III-2-a. Raw data for the summed channel (all de-
tectors) for scan 1 plotted versus ecliptic
latitude. The smooth curve below is the
fitted earthshine function (see Appendix).
The large excess near +30° is due to re-
sidual signal from the nose cone.
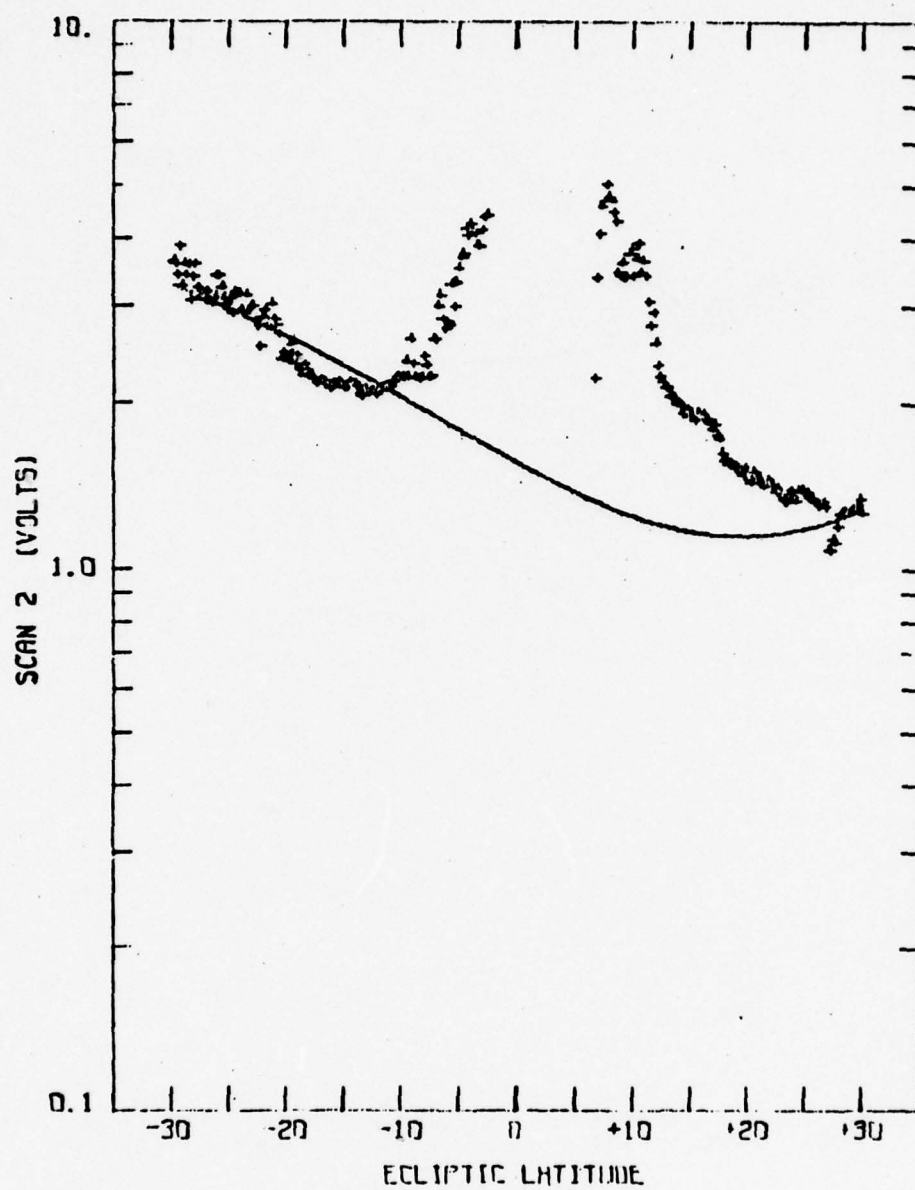
FIGURE III-2-b. Raw data for scan 2.   The gap is caused
by an SD short.

51
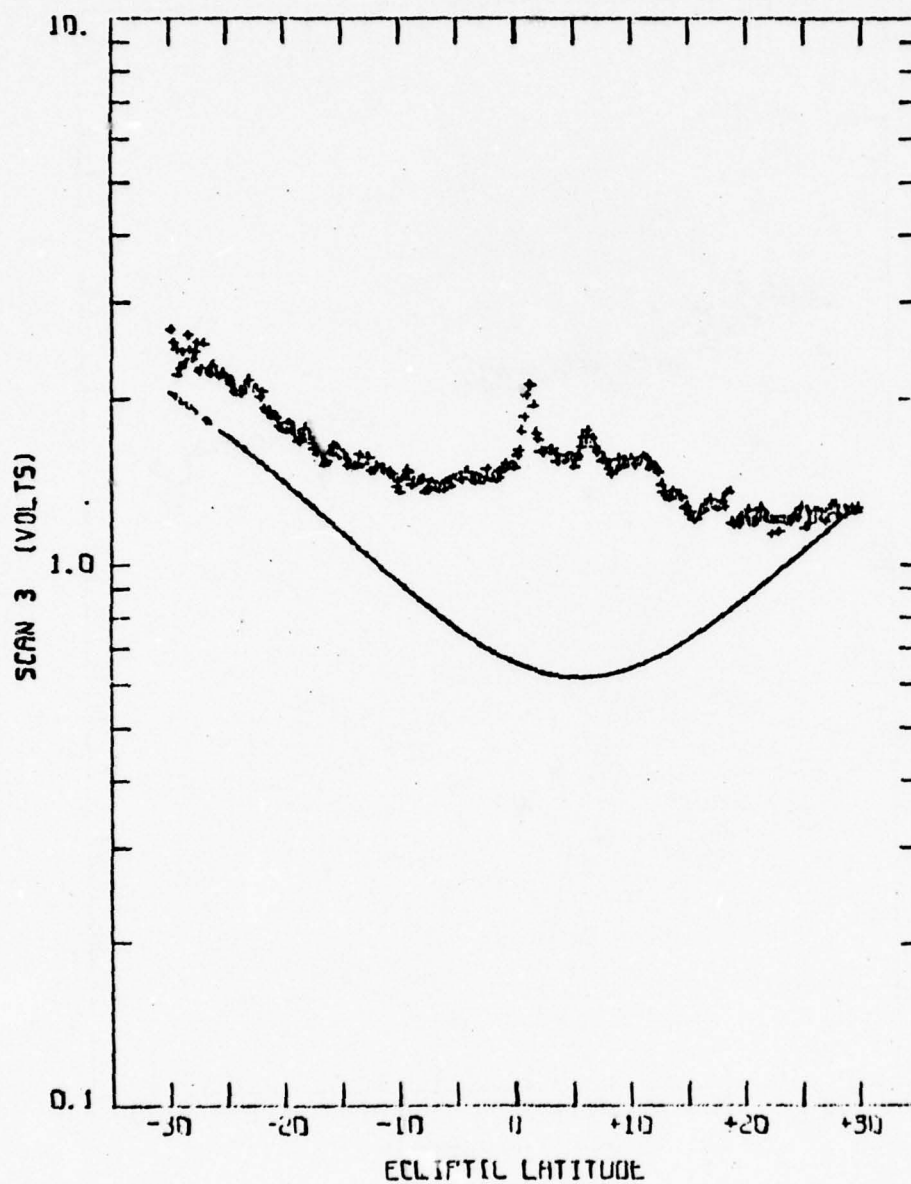
FIGURE III-2-c.   Raw data for scan 3.   The bumps at latitudes of +1° and +7° are believed to be noise spikes.
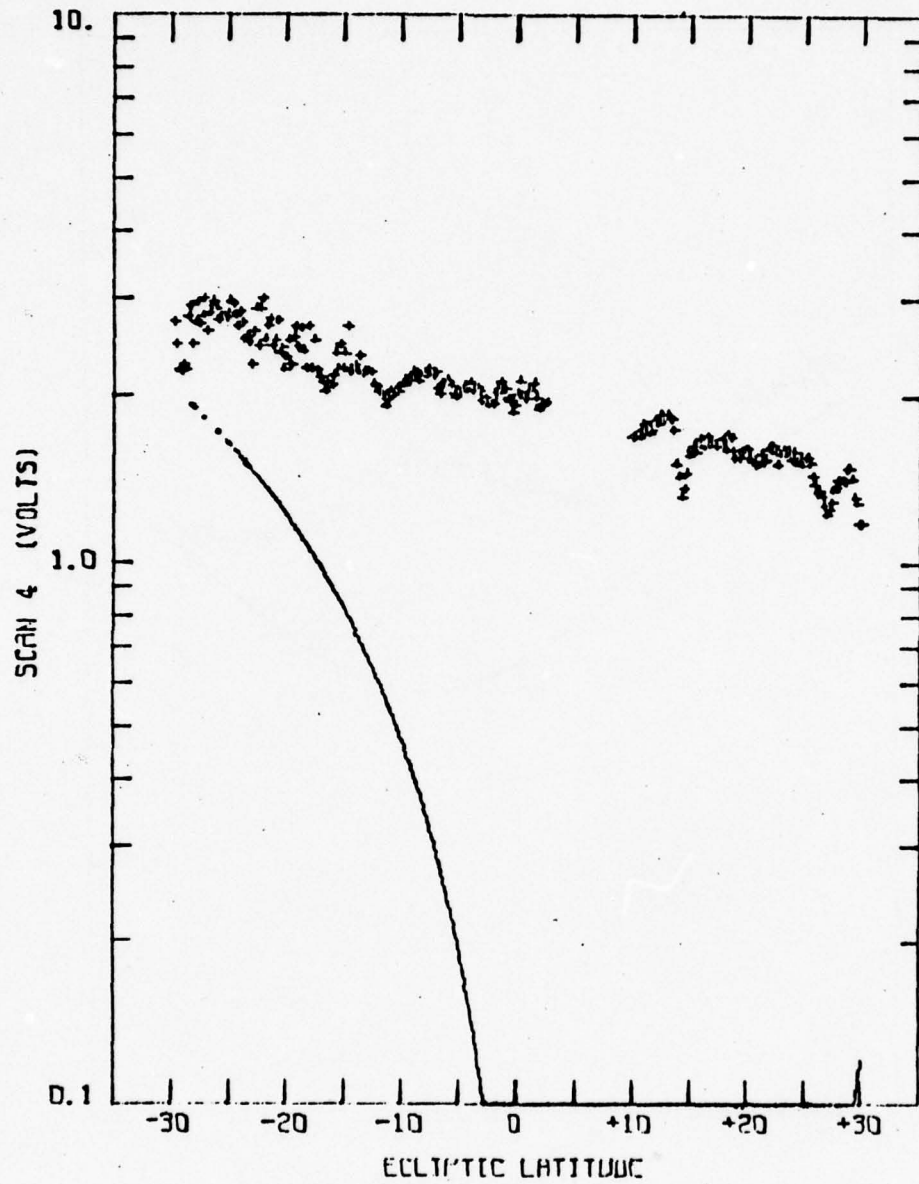
FIGURE III-2-d.   Scan 4 raw data.   The gap is another SD
                   short.   This scan produced the hot blackbody
                   spectrum shown in Fig. IV-2.

FIGURE III-2-e.   Scan 5.   The large, rapidly varying signal
levels are caused by residual exhaust from
the rocket's motor section.

CHAPTER IV

Analysis and Discussion

A. The Spectrum

Because of the noise, all the data in scan 3 that were obviously from the ecliptic dust were averaged together. Essentially this includes data covering apparent latitudes from -5° to $+15^{\circ}$ in Fig. III-2c. The two possible noise spikes in the figure were omitted from the average. The intensity was calculated by:
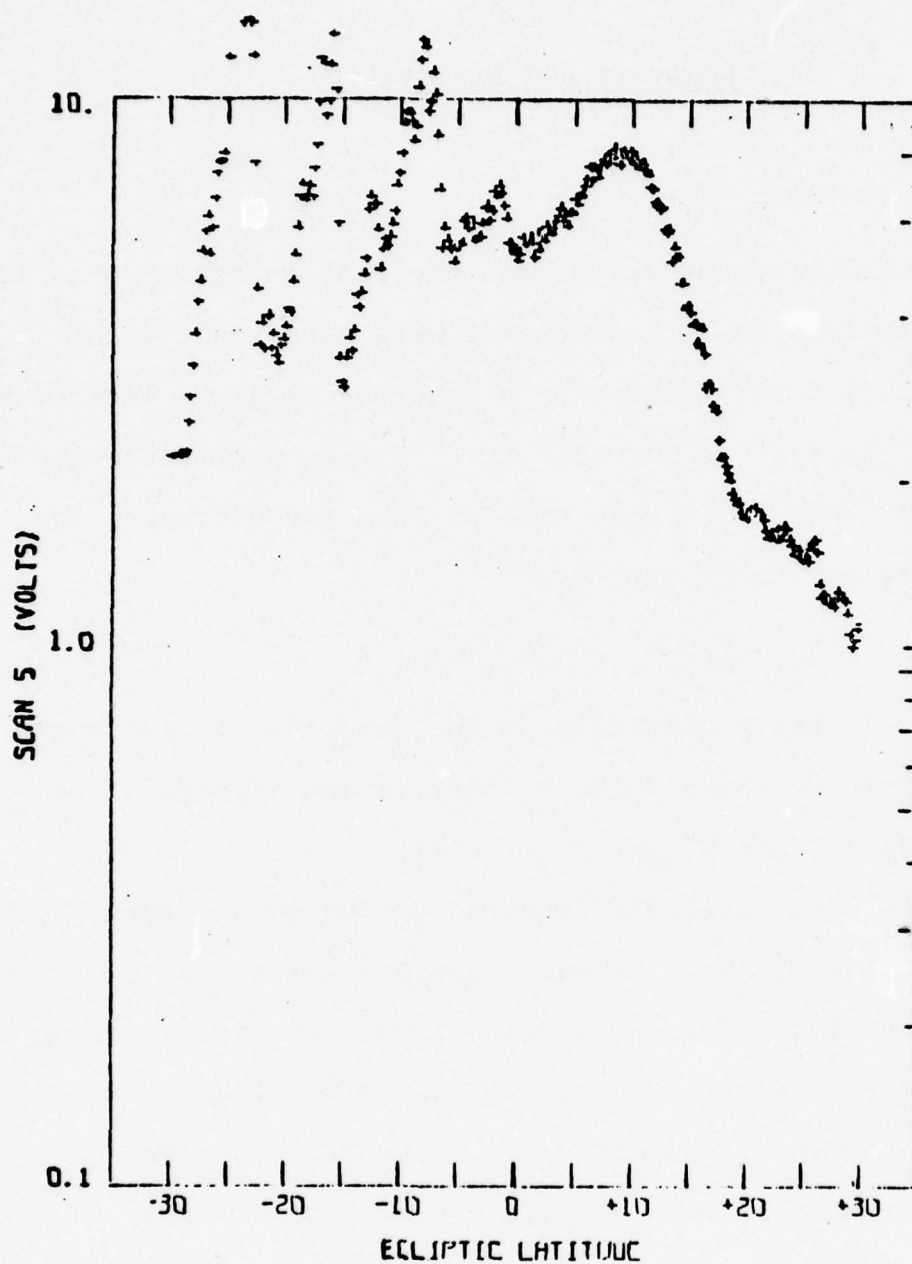
$$I_{\lambda} = R_{\lambda} \ (\overline{V}_{\lambda} - V_{\lambda}^{O})$$

where R_{λ} is the sensitivity of the detector at wavelength λ, in watts/cm^2-sr-μ/Volt, $\overline{V}_{\lambda}$ the average voltage across the ecliptic, and V_{λ}^{O} the zero level.

The zero level was measured in the launch tower just prior to the flight. It was measured over a long period of time ($\sim$ 2 min) and is well determined. SD shorts during this interval were compared with those in flight to make certain the level did not drift. The RMS noise fluctuations during this period, σ_{λ}, give the noise level for any measurement. The noise in $\overline{V}_{\lambda}$ is $\sigma_{\lambda}/\sqrt{N}$, where $N = 88$ is the number of data points averaged, whereas the noise in V_{λ}^{O} is $\sigma_{\lambda}/\sqrt{M}$, where $M = 930$ is the number of points taken in the tower.

The uncertainty in I_{λ} is then given by

54

$$\sigma^2(I_\lambda)/I_\lambda^2 = [\sigma^2(R_\lambda)/R_\lambda^2] + [\sigma^2(\overline{V}_\lambda) + \sigma^2(V_\lambda^0)]/(\overline{V}_\lambda - V_\lambda^0)^2$$

$$= [\sigma^2(R_\lambda)/R_\lambda^2] + [\sigma^2(\overline{V}_\lambda)/(\overline{V}_\lambda - V_\lambda^0)^2]$$

since $\sigma^2(V_\lambda^0) \ll \sigma^2(\overline{V}_\lambda)$.

The spectrum is shown in Fig. IV-1. Blackbodies peaking in this spectral range are much flatter than the observed spectrum, so a silicate feature is apparent. The average level is about 6.5×10^{-11} W/cm^2-sr-μ, consistent with Soifer et al.'s measurement (1971).

Figure IV-2 is the spectrum obtained during scan 4. This spectrum varies approximately as λ^{-4} indicating a hot blackbody, presumably the sustainer scattering in from out of the field of view. This occurred shortly before the residual exhaust becomes visible in scan 5. The high signal levels for detectors #11 ($\lambda = 12.3\mu$) and #13 ($\lambda = 13.1\mu$) are either due to line emission from the hot gaseous component of the exhaust, or else indicate a bad calibration for these detectors. The latter explanation is more likely as these detectors misbehaved in the same direction in the ecliptic spectrum of Fig. IV-1.

B. The Model

The model used to fit the ecliptic spectrum consists of two components: a silicate feature plus an underlying dilute blackbody:

$$I_\lambda = D_1 \overline{Q}_\lambda B_\lambda(T_1) + D_2 B_\lambda(T_2)$$

FIGURE IV-1.   Spectrum of the zodiacal emission seen in
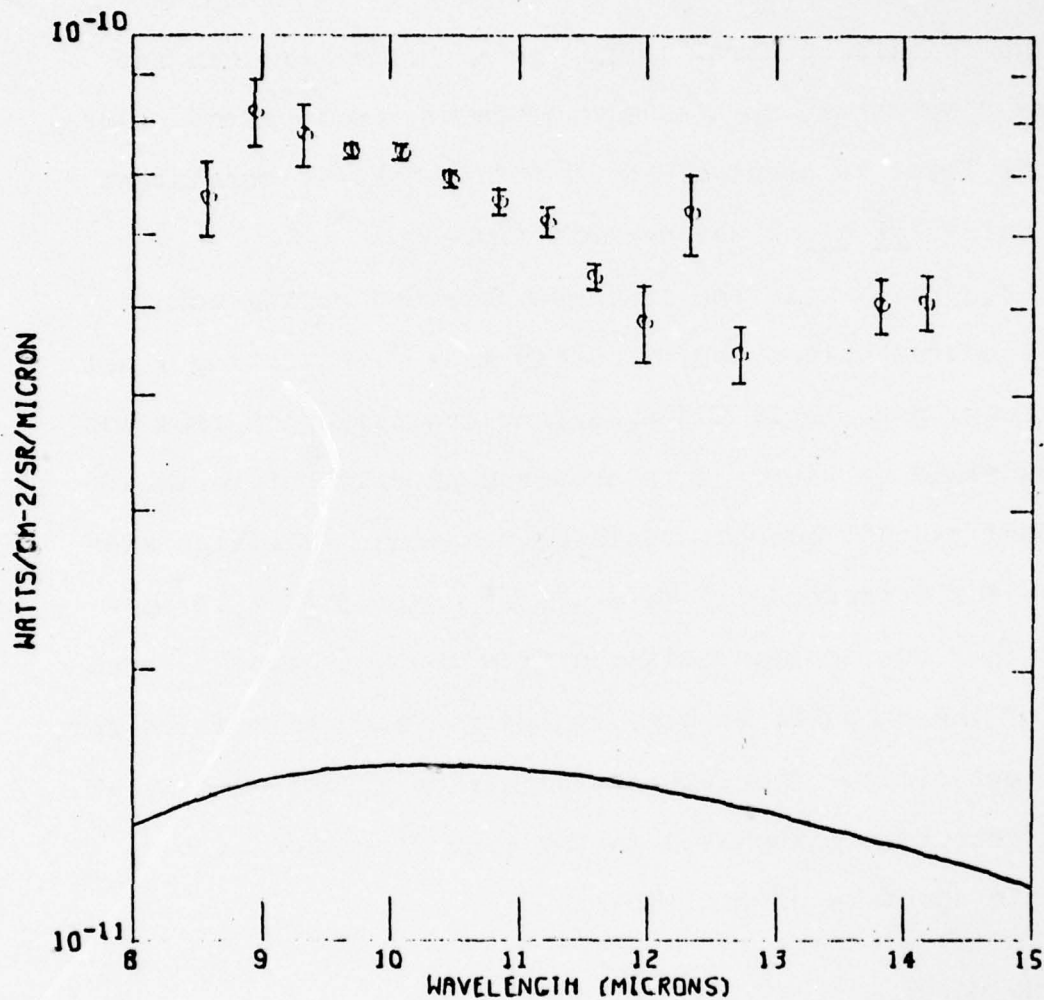scan 3. The intensity for the two points near
14μ is due to the wings of the atmospheric
CO_2 band near 15μ. The lower curve is the
blackbody contribution determined by the chi-
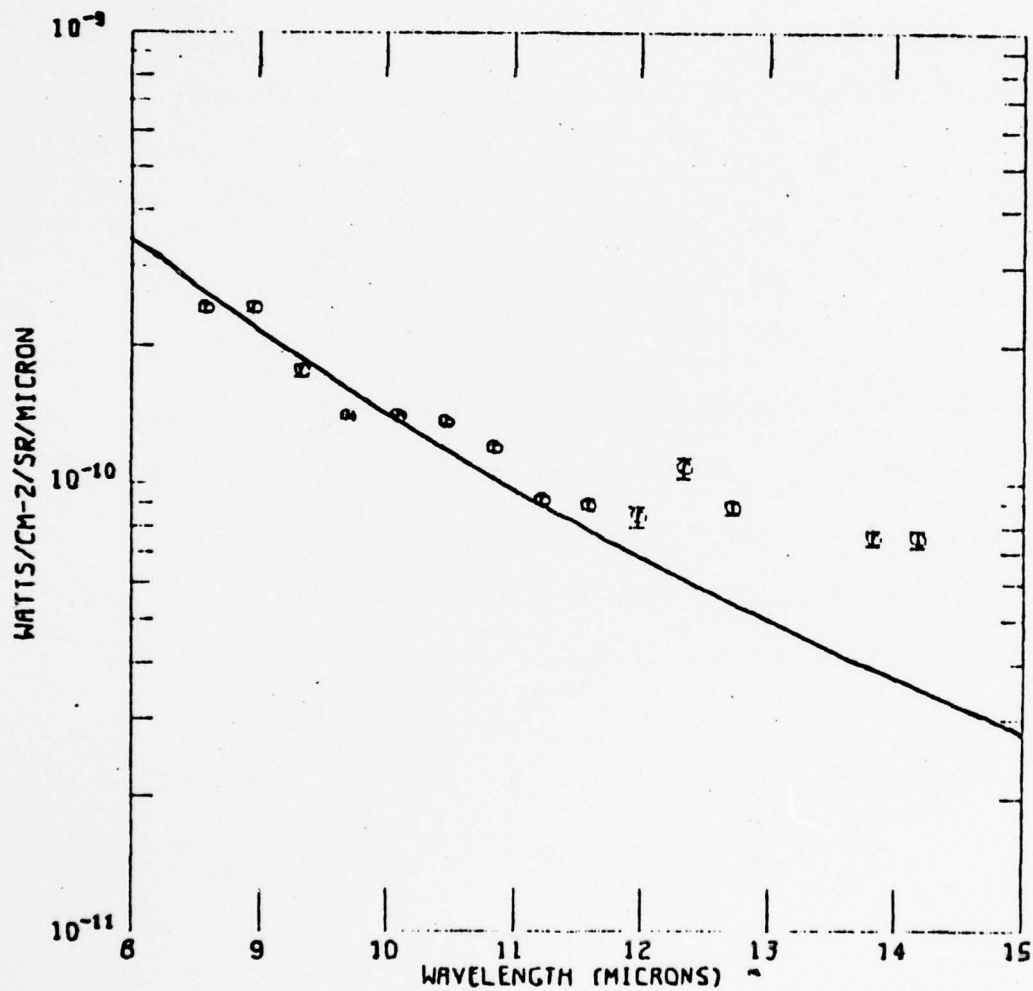squared fit (see text).

FIGURE IV-2. Spectrum observed during scan 4 and attributed to the sustainer. The smooth curve represents a blackbody and is proportional to λ^{-4}.

where $\overline{Q}_\lambda$ is the emission efficiency for the silicate grains averaged over the size distribution for optically thin, i.e. non-blackbody, grains. Optically thick silicate grains and non-silicate grains, which are assumed black, are represented by the second term.

Because of the low optical depth of the cloud, the dilution for the blackbody grains can be written

$$
\begin{aligned}
D_2 &= 1 - e^{-\tau_2} \\
&\simeq \tau_2 \\
&\simeq \iint \pi \, a^2 \, n_2(a) \, da \, dl \\
&\equiv \pi \, \overline{a}_2^2 \, n_2 \, L
\end{aligned}
$$

where $\pi \, \overline{a}_2^2$ is the average cross-section and n_2 the average space density of the blackbody grains. L is the line of sight distance. Since the Pioneer and Mariner observations showed that $n \sim$ constant near the earth, and that it drops sharply beyond 2.25 AU from the sun, L is of the order $L \sim 1$ AU.

Similarly, for the silicate feature we may write

$$
\begin{aligned}
D_1 \, \overline{Q}_\lambda &= \iint \pi \, a^2 \, Q_\lambda(a) \, n_1(a) \, da \, dl \\
&\sim \pi \, \overline{a}_1^2 \, \overline{Q}_\lambda \, n_1 \, L \quad .
\end{aligned}
$$

The emission efficiency may be written

$$
Q(a) = 1 - \exp[-\tau_\lambda(a)]
$$

where $\tau_\lambda(a)$ is the optical depth of a single grain of radius a:

$$
\begin{aligned}
\tau_\lambda(a) &= \int \kappa_\lambda \, \rho_o \, da \\
&= \frac{4}{3} \, a \, \kappa_\lambda \, \rho_o
\end{aligned}
$$

for spherical grains, with κ_λ the mass absorption coefficient and ρ_0 the material density. Taking $\kappa(10\mu) \sim 10^3$ cm^2/gm for small silicate grains, and $\rho_0 \sim 3$ gm/cm^3 (Ney, 1974), the grain optical depth is

$$\tau_\lambda(a) \sim 0.4a(\mu) \; C_\lambda$$

where a is measured in microns, and $C_\lambda = \kappa_\lambda/\kappa(10\mu)$ is the absorption profile. This absorption profile was assumed to have the same wavelength dependence as the emission profile of the grains in the Trapezium measured by Gillett et al. (1975). From their data, C_λ has been calculated and interpolated to the wavelengths of my detectors. It was assumed that the average efficiency $\overline{Q}_\lambda$ over the size distribution may be taken as:

$$\overline{Q} = 1 - \exp[-\tau_\lambda(\overline{a}_1)]$$
$$= 1 - \exp[-0.4 \; C_\lambda \; \overline{a}_1]$$

with $\overline{a}_1$ defined as above.

A χ^2 fit of the observed spectrum to a Trapezium-like silicate feature with an underlying blackbody gave a rather poor fit, $\chi^2/N\text{-}5 \sim 1.5$, mainly due to the bad calibration on detector #11. As a test, detector #11 was recalibrated downwards to fit the λ^{-4} spectrum seen in scan 4. This gave a much better fit, $\chi^2/N\text{-}5 \sim 0.98$, but essentially the same parameters. The best fit values for both calibrations are listed in Table IV-1.

In Fig. IV-1, the spectrum for scan 3, the smooth curve

TABLE IV-1

Results of the χ^2 fit parameters for the

Zodiacal Dust Spectrum.

	Pre-Flight Calibration	Recalibrated #11
Silicate Feature		
Dilution	$1.7 \pm 0.8 \times 10^{-8}$	$2.4 \pm 0.8 \times 10^{-8}$
Temperature	$378 \pm 40\ ^{o}K$	$374 \pm 25\ ^{o}K$
grain radius	4.5 ± 3.7 microns	6.5 ± 2.8 microns
Blackbody Component		
Dilution	$2.7 \pm 1.4 \times 10^{-8}$	$2.1 \pm 1.7 \times 10^{-8}$
Temperature	$321 \pm 38\ ^{o}K$	$284 \pm 71\ ^{o}K$
Goodness of Fit		
$\chi^2/(N-5)$	1.5	0.98

at the bottom is the blackbody contribution $D_2 B_\lambda (T_2)$ from the model fit. The temperature and dilution for the blackbody component have relatively large uncertainties, due to the fact that blackbodies near 300°K are fairly flat in this spectral region. The fit is therefore relatively insensitive to the temperature, compensating for the intensity level by changing the dilution. It is worth noting, however, that the fitted temperature is a reasonable one for blackbodies ~ 1 AU from the sun.

Subtracting the blackbody contribution from the observed spectrum gives the silicate feature in Fig. IV-3. The smooth curve is the χ^2 result for the first term in the fitting function. The fit is pretty good, implying a large silicate contribution to the emission in this spectral region. Furthermore, it is similar to the feature seen in the Trapezium, and, by inference, to the spectrum of the Type I Carbonaceous chondrite measured by Zaikowski and Knacke (1975).

C. Discussion

For the silicate emission component, the fit parameters give the typical grain size as $\bar{a} \sim 5\mu$. From the dilution, the density of silicate grains can be written

$$n_1 \sim \frac{D}{\pi a^2 L} \sim 2.0 \times 10^{-15} / cm^3$$

where L has been taken as 1 AU. The mass density can then be calculated as $\rho_1 \sim 3.2 \times 10^{-24}$ gm/cm^3.
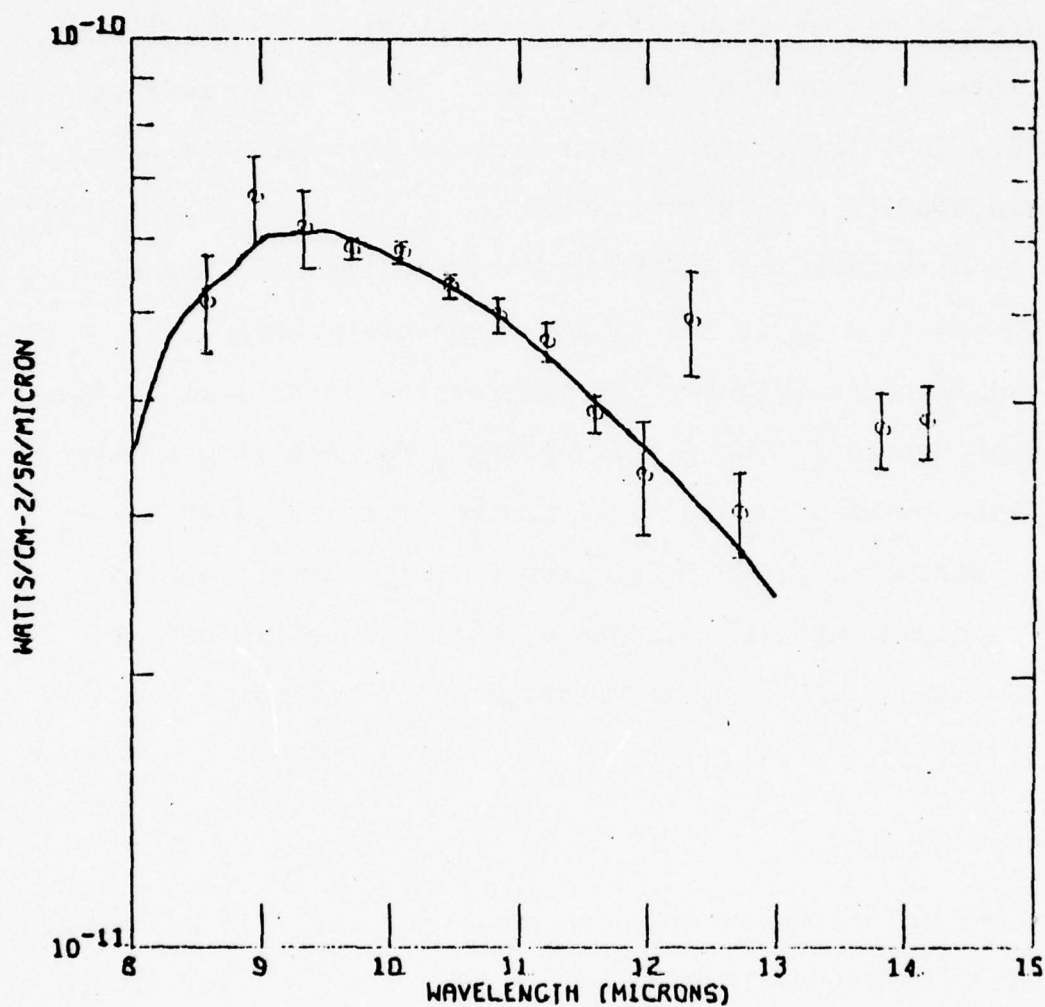
FIGURE IV-3.   Silicate component of the zodiacal dust spec-
trum for scan 3.   The data points are the
spectrum from Fig. IV-1 minus the blackbody
contribution.   The smooth curve is the chi-
squared fit for Trapezium-like silicate
grains.

For the blackbody grains, the typical size cannot
be obtained from the data, but it can be estimated from the
size distribution given by Leinert (1975) and reproduced
in the Introduction to this thesis (Fig. I-1). Beyond a
$\sim 30\mu$, the distribution falls off rapidly, $n(a) \propto a^{-4.2}$,
so grains larger than this will not contribute much to the
emission. If the dominant composition is silicate in nature,
grains smaller than about 10-15μ will show a silicate emis-
sion feature, and hence would not be included in the black-
body term of the fitting function. I therefore take the
average size to be a $\sim 20\mu$. The dilution then gives the
space and mass densities of the blackbody grains as

$$n_2 \sim 1.1 \times 10^{-16} / cm^3$$

and

$$\rho_2 \sim 1.1 \times 10^{-23} gm/cm^3 .$$

Adding the densities for the silicate and blackbody
grains gives

$$n_{tot} = n_1 + n_2 = 2.1 \times 10^{-15} / cm^3$$

and

$$\rho_{tot} = \rho_1 + \rho_2 = 1.4 \times 10^{-23} gm/cm^3$$

For comparison, the Pioneer 10 data (Humes et al., 1974)
measured $n \sim 10^{-15}/cm^3$. For the mass density, Allen (1964)
gives $\rho \sim 3 \times 10^{-23} gm/cm^3$ and Leinert (1975) gives
$\rho \sim 4 \times 10^{-23} gm/cm^3$.

Although the temperature for the blackbody grains is
reasonable, the temperature for the grains small enough to
show a silicate feature seems high. The temperature of a
grain at a distance r from the sun and with an albedo A is:

$$T_g = 280^\circ K \ (r_o/r)^{1/2} \ (1-A)^{1/4} / \langle Q_{em} \rangle^{1/4}$$

where $\langle Q_{em} \rangle$ is the mean of the emission efficiency over the Planck function for the grain temperature. Taking $r \sim 1$ AU and $T_g = 375^\circ$K gives:

$$\langle Q_{em} \rangle \sim 0.3 \ (1-A) \quad .$$

For $A \sim 0.3$, this gives $\langle Q_{em} \rangle \sim 0.2$. This seems low for grains as big as the model fit would indicate and possibly indicates the presence of smaller, hotter grains that contribute significantly to the observed spectrum. The calculations of Knacke and Thompson (1973) for the Q values of lunar silicate grains would also suggest a size more the order of 0.5 to 1μ.

The presence of such a strong greenhouse effect is in contradiction to the opposite effect predicted for pure olivine spheres by Gilman (1974). The zodiacal dust is almost certainly not pure olivine, and whether a greenhouse or an inverse green house effect controls the temperature of the grains will depend on the composition of the material. The presence of impurities may alter the radiative properties significantly. Knacke and Thompson have shown that for lunar silicates, the relative strength of the 18μ band to that of the 10μ band increases as the FeO content increases and the SiO_2 and Al_2O_3 contents decrease. Further observations of both these bands should help identify the mineralogical nature of the zodiacal dust.

D.   Conclusions

The 8-14 micron spectrum of the zodiacal dust shows
a strong silicate emission feature at 10μ, similar to those
seen in the Orion Nebula and in Type I carbonaceous chon-
drites.   The strength of the feature indicates a typical
grain size the order of 5μ, although larger blackbody grains
and possibly smaller, hotter silicate grains may also con-
tribute to the emission.   The dilutions are consistent with
the particle and mass densities observed by others.   The
temperatures indicate a strong greenhouse effect for the
smaller particles.   The presence of the 10μ feature suggests
that observations in the 18μ silicate band could identify
the mineralogical composition of the dust.

CHAPTER V

Far Infrared Observations

A. Instrument

The optical configuration of the far infrared spectro-
meter is identical to the near infrared system (Briotta, 1976)
except that the 1" Bausch and Lomb aluminum grating was ruled
to 6 lines/mm and blazed for 80μ. The six individual far in-
frared detectors were placed so the vertical astigmatic focus
lay along the slit length, and alignment procedures for the
near and far infrared systems were identical.

The six photo conductors employed were arranged so that
the three longest wavelength detectors received 1st order dif-
fracted radiation and the three shortest wavelength detectors
received 2nd order diffracted radiation. The five longest
wavelength detectors were fabricated out of Ge:Ga by J. Pipher
(see Moore and Shenker, 1965) for a description of the boole
properties, and the shortest wavelength, detector was fabri-
cated out of a Ge:Cu boole (Quist, 1968) by Robert Reed. A
quartz filter with a laminated interference layer of poly-
ethylene (Armstrong and Low, 1974) and a KI filter separated
orders and a black polyethylene filter was used to reject
radiation that would activate the intrinsic response of the
photo conductors. The aperture size at the detector was
0.35cm x 0.4cm. The detector wavelength responses are listed
in table V-I.

The detector preamplifiers and synchronous demodulators have been described previously (eg. Pipher, 1971) and were used on past Cornell University rocket flights.

B. Calibration

The far infrared package was calibrated using a liquid nitrogen blackbody, specially developed for rocket payloads. This blackbody, in the form of a lid replacing the flight cover during calibration, allows variable small apertures in a cold ($\sim 10^{\circ}$K) shiny copper plate to sample radiation from a copper cavity filled with liquid nitrogen, and covered on the visible (by the detectors) portion of the cavity with cryogenic black paint (Pipher and Houck, 1971). The detector system NEP's (noise equivalent power) are also shown in Table V-I.

C. Flight

As described in detail earlier, a 60° sawtooth scan across the median ecliptic plane was employed. Scan 1 and most of 2 were contaminated by signals from the nose cone. After scan 4 the signals began to rise and fluctuate, and it is proposed that the separated sustainer engine was the source of this difficulty. Hence scans 3 and 2 (perhaps) are the only source of reliable data on the flight.

Of the six far infrared channels, channels 1 and 6 malfunctioned. The signal levels during scan 3 obtained with the four remaining operational detectors are reported below.

D. Observations

In Table V-II we list the minimum signals observed during the flight by the operative detectors. These were obtained during scan 3, at a zenith angle of 30°, a galactic latitude of 23° and an ecliptic latitude of 25°. As described by Briotta, the baffles designed to minimize earthshine correction to the experimental data were modified to leave the outermost diffraction baffle shiny (to prevent heating of the baffle) instead of blackening it (as designed). This resulted in an earthshine correction that was not optimum: the minimum signal levels reported are close to the calculated values of the earthshine correction assuming the modified baffling function as a function of zenith angle. This function is displayed by Briotta in the appendix of this report.

During scan 3, both the ecliptic and galactic planes were crossed at zenith angles of 22° and 27° respectively. In each crossing case the latitude of the other plane was $\sim 10^{\circ}$. At the longest wavelengths, diffuse radiation from the galactic plane is expected to contaminate zodiacal particle radiation measurements (Pipher, 1971).

The minimum detectable signals levels observed on this scan are only facotrs 2-6 time the NEFD (noise equivalent flux density). Hence averages over one second of data (2° on the raster) were taken to estimate radiation from zodiacal particles. In table V-III we show the measured signal level and the signal level expected from the measurements of Soifer et al.

(1971) on the assumption that a dilute 280°K blackbody is appropriate. Although absolute calibration errors are difficult to assess, and although we are operating in the low signal to noise regime, there is fair agreement at $\lambda = 39$ and 46μ.

Channels 4 and 5 ($\lambda = 62, 77\mu$) are sensitive to diffuse emission from the galactic plane. The signal levels encountered at $b^{II} = 0$, averaged over one sec as before, are for channels 4 and 5.2 x 10^{-12} and 3 x 10^{-12} watts/cm^2-sr-μ respectively, in reasonable accord with expectations from past measurements (Pipher, 1973).

Although the low signal to noise makes model fitting of the sort described in this reference impractical, it is clear that half or more of the radiation measured by longest wavelength detectors as the ecliptic plane emission. Our results, then suggest a dilute 280°K blackbody emission from zodiacal dust particles, although a faster fall-off in wavelength at $\lambda > 60\mu$ would also fit the observations.

TABLE V-1

Far Infrared Detector Properties

Channel	$\lambda(\mu)$	NEP (watts/$(Hz)^{\frac{1}{2}}$)
1	26-35	8.3×10^{-12}
2	35-43	8.9×10^{-13}
3	43-49	3.8×10^{-13}
4	55-70	1.4×10^{-13}
5	70-85	1.4×10^{-13}
6	85-110	1.85×10^{-13}

TABLE V-2

Minimum Detected Signals

Channel	Signal (watts/$cm^2 sr \mu$)
2	1.2×10^{-11}
3	4.2×10^{-12}
4	5.3×10^{-12}
5	1.3×10^{-12}

TABLE V-3

Zodiacal Dust Radiation

Channel	$\lambda_m(\mu)$	Measured Signal	Expected Signal
		(watts/cm^2-sr-μ)	
2	39	7.5×10^{-12}	$2. \times 10^{-12}$
3	46	3.8×10^{-12}	1.1×10^{-12}
4	62	$3.5 \times 10^{-12}*$	$6. \times 10^{-13}$
5	77	$1.6 \times 10^{-12}*$	2.5×10^{-13}

*contaminated by diffuse radiation from galactic plane

APPENDIX

Baffle Design and the Earthshine Correction

A. Baffle Design

Two assumptions were made in the design of the diffraction baffles. The first is that the radius of curvature of the cylindrical baffles is large compared to a wavelength. The second is that the earthshine striking the baffles is a plane wave. Under these assumptions, the earthshine around a baffle can be modeled as simple scalar diffraction by a straight edge. Thus the ratio of intensity I_1 at any point in the shadow to the incident intensity I_0 is given by:

$$S = \frac{I_1}{I_0} = (1/2) \left\{ [0.5 - C(w)]^2 + [0.5 - S(w)]^2 \right\}$$

$$\sim 1/(4 \pi w^2) \text{ in the shadow,}$$

(Landau and Lifschitz, 1962) where $C(w)$ and $S(w)$ are Fresnel integrals, $w = h \sqrt{\pi/\lambda D}$, and h and D are defined in Fig. A-1. The actual angle of the baffle is unimportant, i.e. the diffraction is an edge phenomenon depending only on the position of the edge (Baker and Copson, 1950). Thus, when light strikes the baffle at an angle θ to the horizontal, D is measured along the original ray direction, and h perpendicular to it. (Fig. A-2)

Given the array of baffles in Fig. A-3, the intensity striking the ith baffle is a function of $D_i = \Delta x_i \cos \theta_i +$
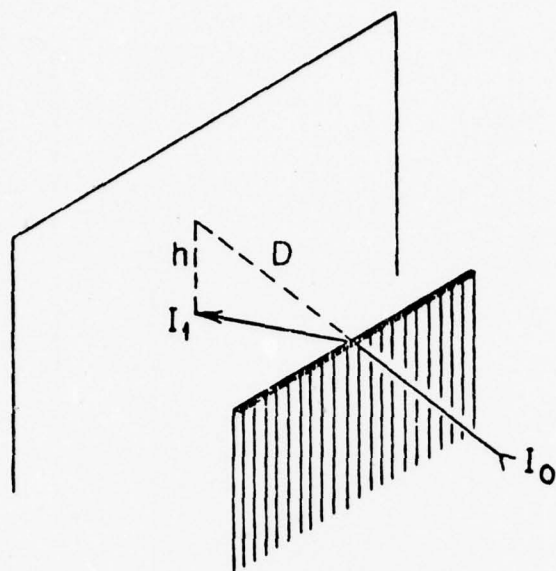
72

FIGURE A-1. Geometry for simple scalar diffraction. D is measured along the original ray direction, and h is perpendicular to it.
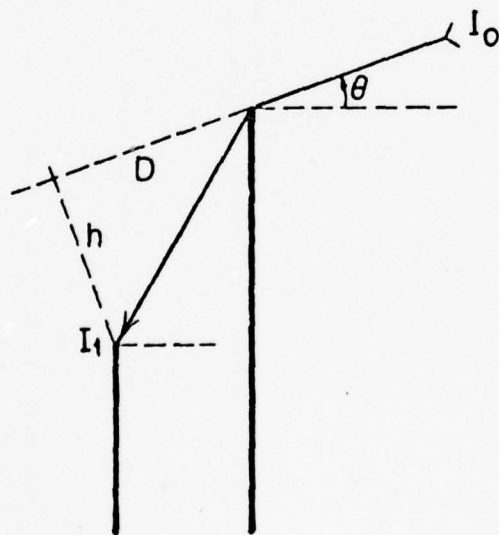

FIGURE A-2. Geometry for oblique incidence. D and h are measured as before.

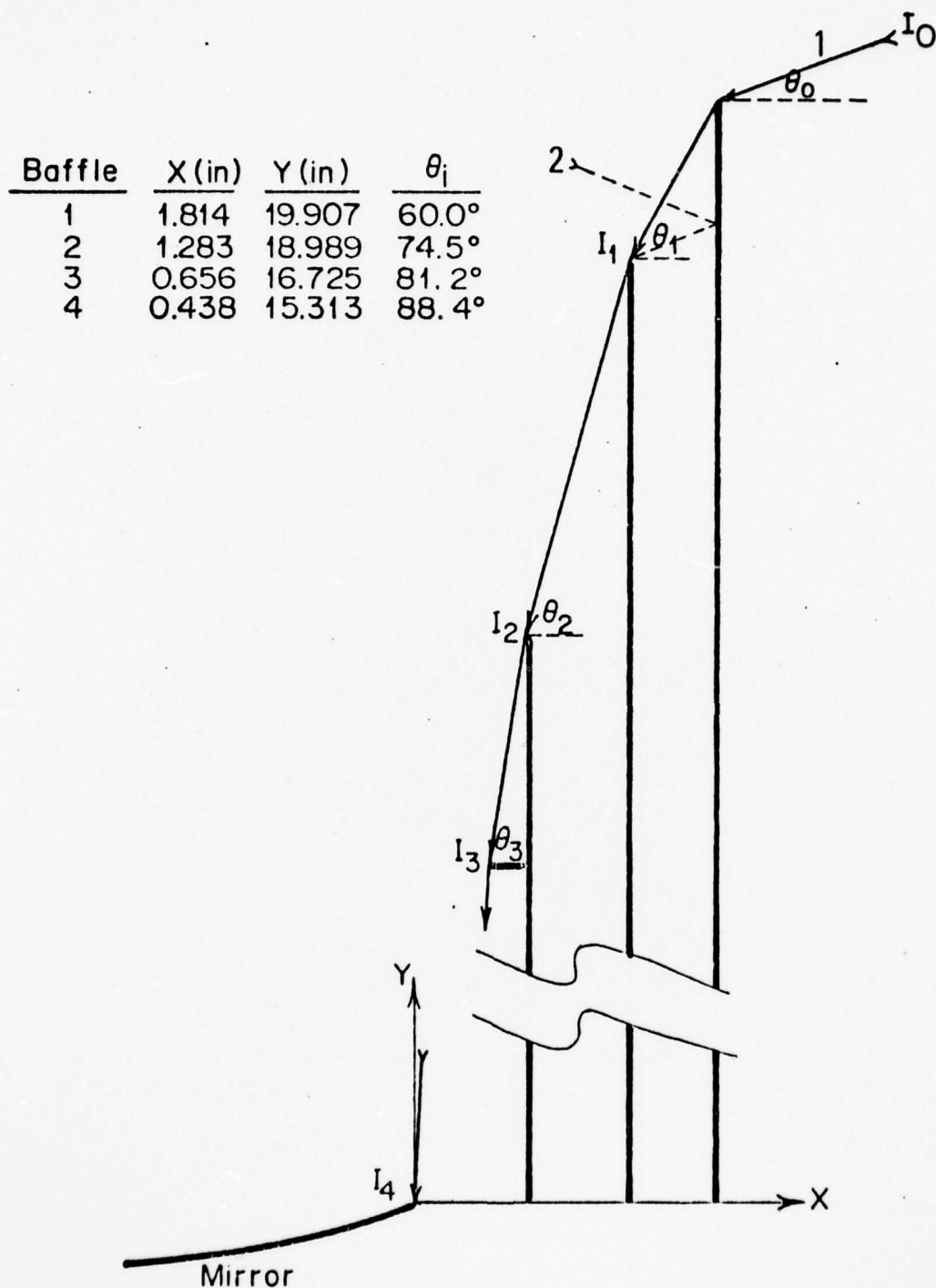| Baffle	X(in)	Y(in)	θ_i
1	1.814	19.907	60.0°
2	1.283	18.989	74.5°
3	0.656	16.725	81.2°
4	0.438	15.313	88.4°

FIGURE A-3. Drawing of the diffraction baffles. The table lists the positions of the edges, measured from the edge of the primary mirror. Ray #1 is the nominal ray used for the design. Ray #2 shows a possible reflection off the shiny inner surface of the outermost baffle.

$+ \Delta y_i \sin \theta_i$ and of $h_i = -\Delta x_i \sin \theta_i + \Delta y_i \cos \theta_i$, given by:

$$S(\theta_i) = I_i/I_{i-1} \simeq \lambda \, D_i/(4 \, \pi^2 \, h_i^2) \propto D_i/h_i^2 \quad .$$

The telescope mirrors were polished to a special low scattering surface, scattering less than 10^{-5} of the intensity of rays $> 1^{\circ}$ off axis into the beam. Dust on the surface of the mirrors, however, can degrade this performance by one or two orders of magnitude, and care was taken to protect the surfaces as much as possible. The diffracted ray most likely to enter the beam must strike the edge of the mirror, since then its direction is closest to the optical axis. If we define $S(\theta_i) \equiv D_i/h_i^2$, then at the edge of the mirror (point 4 in Fig. A-3) the intensity is

$$I_4 \propto S(\theta_0) \, S(\theta_1) \, S(\theta_2) \, S(\theta_3) \quad .$$

The design procedure was to adjust the positions of the baffles to minimize the intensity at the edge of the mirror over the widest range of θ_0, which is the only angle that changes in flight, and depends on the telescope orientation with respect to the earth. This is an iterative procedure, and precise criteria cannot be given for a "good" baffle configuration. For any configuration the diffraction profile can be calculated as a function of θ_0. Such profiles were calculated for various numbers and positions of the baffles. Constraints on these parameters were provided by the available room between the inner dewar wall and the edge of the rocket skin, and by the recessed distance of the mirror edge from the front of the skin. The choice of a

"better" configuration was largely a subjective one, the main criterion being a lower profile for $\theta_0 < 60^0$.

The positions of the baffles chosen for the flight are given in Fig. A-3. The origin is the edge of the mirror. The corresponding diffraction profile is shown in Fig. A-4. When the angle θ_0 approaches θ_1 there is a steep rise in the intensity as the first baffle becomes less effective and we approach the edge of its shadow. In this region, the simple approximation given above is invalid, and the full Fresnel integrals must be calculated. An approximation for them, given by Boersma (1960) was used. When $\theta_0 > \theta_1$, light strikes the second baffle directly and the first baffle is discarded. This effect is repeated for $\theta \sim \theta_2$, etc.

B.   The Earthshine Correction

In flight, the peak altitude reached was A = 165.2 nautical miles. From Fig. A-5, the horizon depression is:

$$HD = \cos^{-1}[R_e/(R_e + A)] = 17.4^0 ,$$

where R_e is the radius of the earth. If the telescope is oriented with a zenith angle of ZA, we have:

$$\theta_0 = 90^0 - (90^0 - ZA + HD)$$
$$= ZA - HD .$$

The maximum zenith angle reached during flight was ZA $\sim 60^0$. Thus

$$\theta_0 < 43^0 < \theta_1 = \tan^{-1}(h_1/D_1) = 60^0.$$

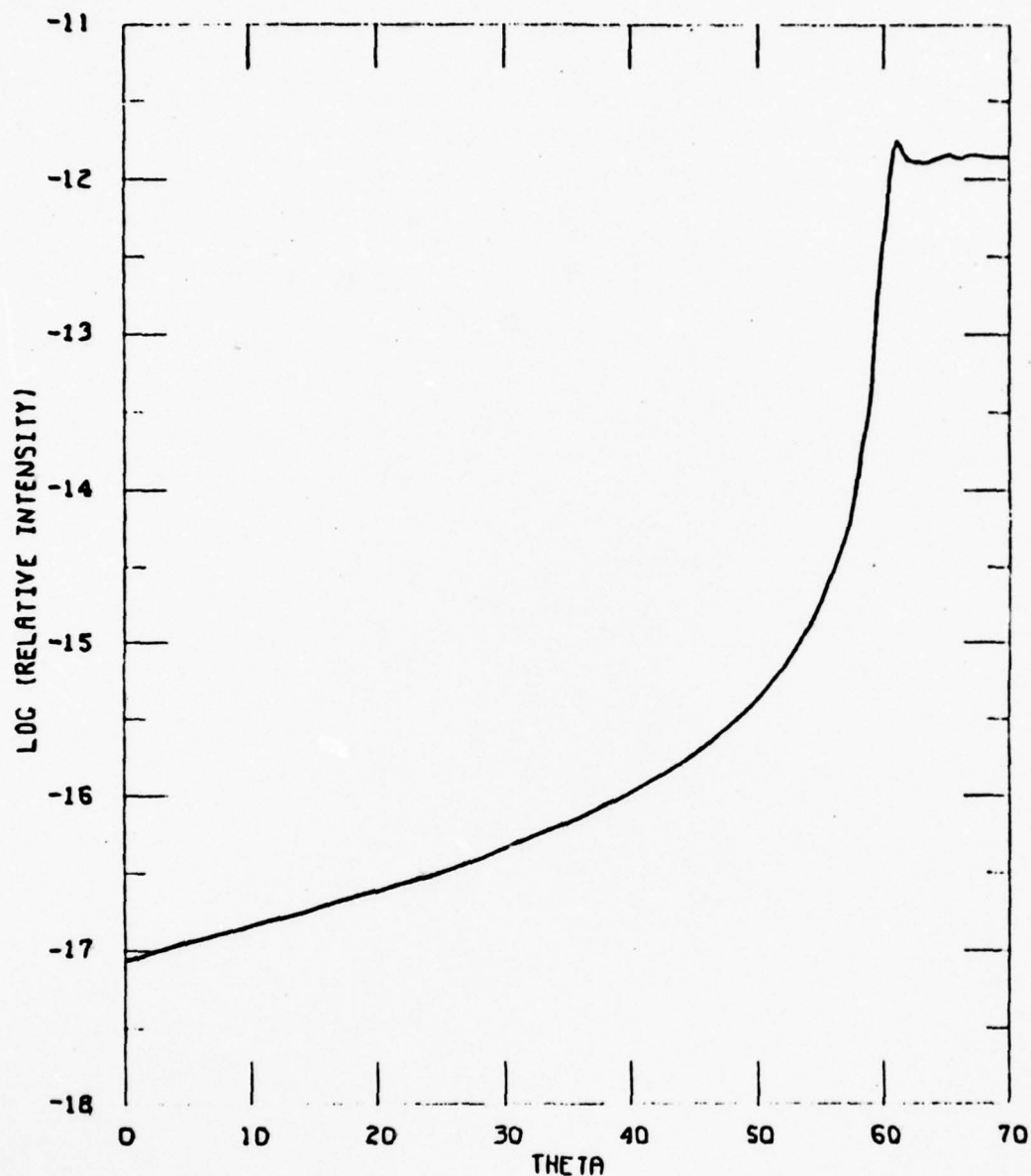As long as this remains true, the diffracted light reaching

FIGURE A-4. Diffraction profile for the baffles in Fig. A-3, for Ray #1. This was calculated for $\lambda = 10.08\mu$ (i.e. detector #5). Note the large increase in intensity as light begins to illuminate the edge of the second baffle directly.
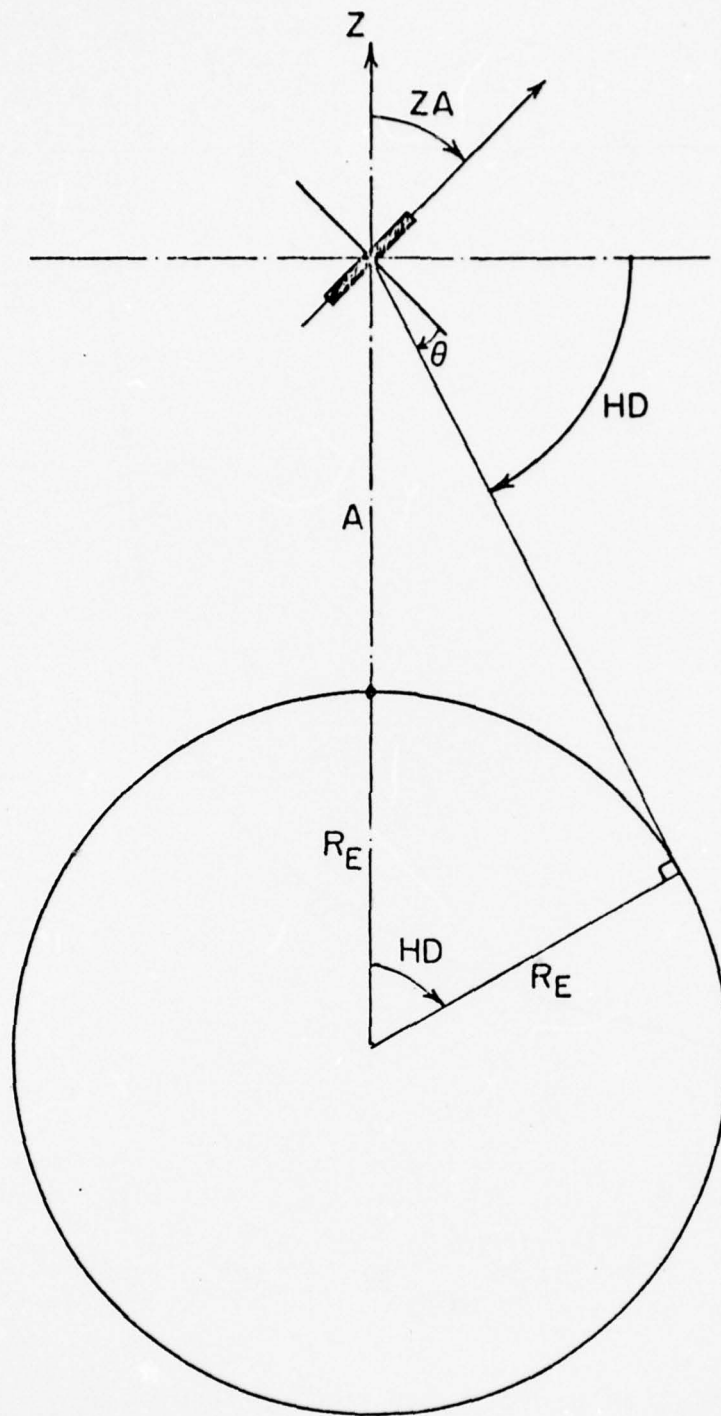
FIGURE A-5. Geometry for the diffraction beam integral.
A is the rocket's altitude, ZA is the zenith
angle of the telescope, and HD the horizon
depression.

the other baffles, or any other diffracting edge such as
the secondary support tripod, must come from the edge of
the second baffle after diffracting past the outer one.
Since the positions and diffraction angles are constant be-
yond this point, the intensity of light striking the mirror
from any diffraction path will always be a constant times the
intensity at the edge of the second baffle. The contribution
of all such paths can be lumped together into one constant,
and we have

$$I_4 = K \, S(\theta_0) \quad .$$

Diffraction from the first to the second baffle controls
the shape of the profile, while diffraction after that con-
trols the overall intensity.

The beam pattern of the telescope is the axially sym-
metric rotation of this profile about the rocket, i.e.
optical, axis: $B(\theta, \phi) = k \, S(\theta)$.

At a zenith angle of ZA, and with a horizon depression
of HD, the solid earth fills a portion of the beam defined by:

$$E(\theta, \phi) = E^0 \qquad \text{for } -90^o < \theta < \theta_e(\phi)$$
$$= 0 \qquad \text{otherwise,}$$

where $\theta_e(\phi) \equiv -HD + ZA \cos(\phi)$. The total earthshine at any
ZA is then given by (Kraus, 1966)

$$E(ZA) = \iint_{2\pi} K \, S(\theta) \, E(\theta, \phi) \, d\Omega$$

$$= K \, E^0 \iint_{0 < \theta_e} S(\theta) \, d\Omega \quad .$$

The scale factor, K E^O, was determined by fitting the calculated E(ZA) to that observed in flight.

After the baffles were designed, it was decided to leave the inside surface of the outermost diffraction baffle shiny, instead of blackening it as described for the other baffles in Chapter II. This was to prevent earthlight that strikes the baffle directly from heating it up, and causing it to radiate. Leaving the baffle shiny, however, permits light to reflect off of it, and strike the second baffle with little attenuation, e.g. ray #2 in Fig. A-3. When this ray is included in the diffraction profile, the resulting beam integral shows a steep rise in diffracted intensity (Fig. A-6, upper curve) for zenith angles greater than about 21°. However, both diffraction patterns, with and without the reflected ray, have about the same zenith angle dependence, $\propto ZA^{2.1}$, beyond about ZA = 30°. Since scan 3, which contained the only useful data, occurred entirely in this region, and since the absolute diffracted intensity is fit to the data, both patterns will give the same earthshine correction for scan 3. The decision to leave the outer baffle shiny is admitted to be a design error, as the earthshine contribution could have been greatly reduced by painting the baffle.

Calculations of the earthshine correction were also made assuming the radius of the earth to be 100 km larger, to estimate the effect of the airglow layer observed at that altitude. The only significant change was a slight
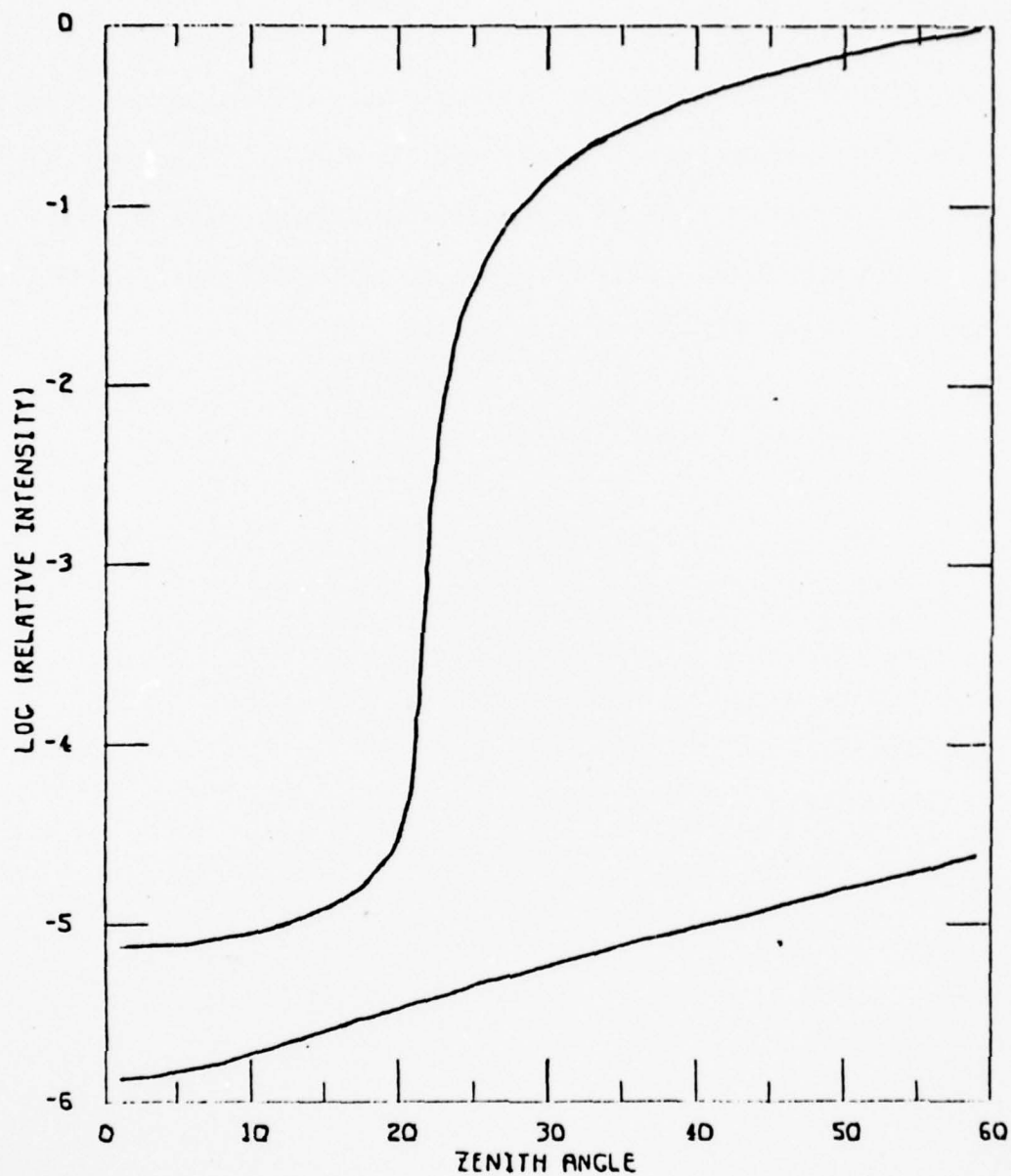
FIGURE A-6. Beam integral for the earthshine correction. The lower curve is for ray #1, as designed. The upper curve is for the reflected ray (#2). The units are arbitrary.

shift towards the zenith of the steep rise in earthshine due to the reflected ray. As this did not affect the corrections for Scan 3, it is considered unimportant.

Figure A-7 shows the increase in earthshine observed during the turnaround between scans 1 and 2. The smooth curve below it is the calculated earthshine correction. For a comparison of the calculations with the rest of the data, see Figs. III-2a-2e in Chapter III.
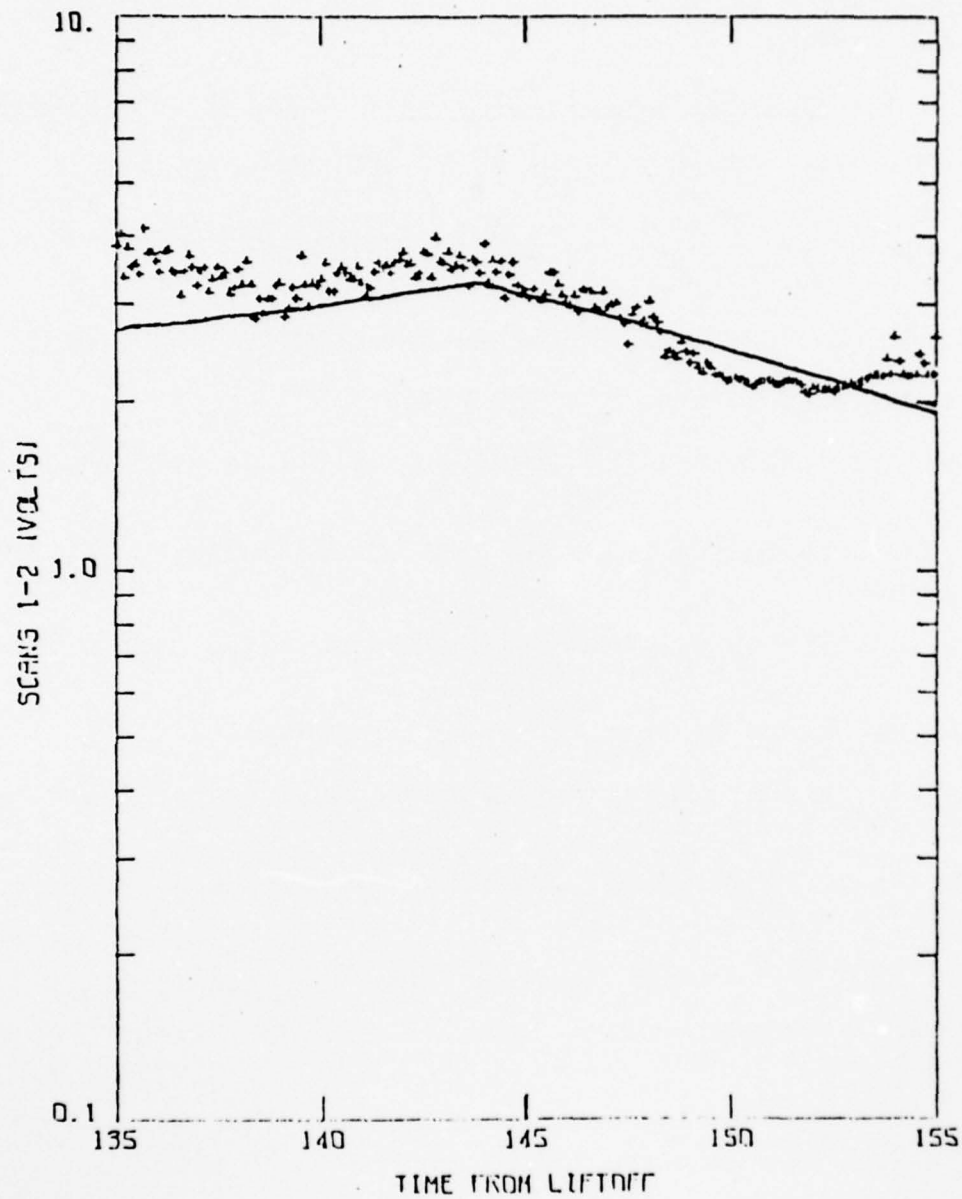
FIGURE A-7. Raw data for the summed channel between scans 1 and 2. The bump from T+140 to T+148 is due to earthshine. The smooth curve is the earthshine function from Fig. A-6.

REFERENCES

Alexander, W.M., McCracken, C.W., and Bohn, J.L., Science, 149, 1240 (1965).

Allen, C.W., Astrophysical Quantities, Athlone Press (1964).

Armstrong, K.R. and Low, F.J., 1974, App. Opt. 13, 425.

Baker, B.B., and Copson, E.T., The Mathematical Theory of Huygens' Principle, 2nd edition, Clarendon Press (1950), pp. 84-92.

Berg, O.E., and Grun, E., Space Research XIII, 1047 (1973).

Boersma, J., Math. Comp. 14, 380 (1960).

Burnett, G.B., Sparrow, J.G., and Ney, E.P., Nature, 249, 639 (1974).

Dumont, R., and Sanchez, F., Astron. and Astrophys., 22, 321 (1975).

Frey, A., Hoffmann, W., Lemke, D., and Thum, C., Astron. and Astrophys., 36, 447 (1974).

Giese, R.H., Space Research III, 1165 (1973).

Giese, R.H., Hanner, M.S., and Leinert, C., Planet. Space Sci., 21, 2061 (1973).

Gillett, F.C., Forrest, W.F., Merrill, K.M., Capps, R.W., and Soifer, B.T., Ap.J., 200, 609 (1975).

Gilman, R.C., Ap.J. Supp. #268, 28, 397 (1974).

Hanner, M.S., Weinberg, J.L., DeShields, L.M., Green, B.A., and Toller, G.N., JGR, 79, 3671 (1974).

Hopkins, R.E. and Hanau, R., "Fundamental Methods of Ray Tracing", Section 5 in Optical Design, MIL-DHBK-141 (1962).

Humes, D.H., Alvarex, J.M., O'Neal, R.L., and Kinard, W.H., JGR, 79, 3677 (1974).

James, J.F., and Sternberg, R.D., The Design of Optical Spectrometers, Chapman and Hall, Ltd., (1969).

Kaiser, C.B., Ph.D. dissertation, Univ. of Colo., NCAR Coop. Thesis #10 (1968).

Knacke, R.F., and Thompson, R.K., PASP, 85, 341 (1973).

REFERENCES (cont'd)

Kraus, J.D., Radio Astronomy, McGraw-Hill (1966), pp. 59-65.

Landau, L.D., and Lifshitz, E.M., The Classical Theory of
Fields, Addison-Wesley, 2nd edition (1962), Sec. 60,
pp. 172-175.

Leinert, C., Space Sci. Rev., 18m 281 (1975).

Lindblom, P., JOSA, 62, 756 (1972).

Merrill, K.M., Icarus, 23, 566 (1974).

Moore, W.J. and Shenke, H., 1965, Infrared Physics, 5, 99.

Ney, E.P., Icarus, 23, 551 (1974).

Pipher, J.L., CRSR Report 461, 1971.

Pipher, J.L. and Houck, J.R., 1971, App. Optics 10, 567.

Pipher, J.L. (in preparation).

Pipher, J.L., 1973, Interstellar Dust and Related Topics,
ed. Greenberg and van de Hulst, p. 559.

Quist, T.M., 1968, Proc. I.E.E.E. 56, 212.

Rhee, J.W., Berg, O.E., and Richardson, F.F., Geophys. Res.
Lett., 1, 345 (1974).

Robley, R., Astron. and Astrophys., 41, 385 (1975).

Soberman, R.K., Neste, S.L., and Lichtenfeld, K., JGR, 79,
3685 (1974).

Soifer, B.T., Ph.D. Thesis, Cornell Univ., CRSR report
#503 (1972).

Soifer, B.T., Houck, J.R., and Harwit, M., Ap.J., 168.
L73 (1971).

Sparrow, J.G. and Ney, E.P., Ap.J., 174, 705 (1972).

Staude, H.J., Astron. and Astrophys., 39, 325 (1975).

Weinberg, J.L., Ann. Astrophys., 27, 718 (1964).

Wolstencroft, R.D., and Rose, J.L., Ap.J., 147, 271 (1967).

Zaikowski, A., and Knacke, R.F., Astron. Space Sci., 37. 3
(1975).